LETTER

https://doi.org/10.1038/s41586-019-1185-4

An ultra-stable gold-coordinated protein cage displaying reversible assembly

Ali D. Malay[1,14], Naoyuki Miyazaki[2], Artur Biela[3,4], Soumyananda Chakraborti[3], Karolina Majsterkiewicz[3,5], Izabela Stupka[3,5], Craig S. Kaplan[6], Agnieszka Kowalczyk[3,7], Bernard M. A. G. Piette[8], Georg K. A. Hochberg[9,15], Di Wu[9], Tomasz P. Wrobel[10], Adam Fineberg[9], Manish S. Kushwah[9], Mitja Kelemen[11,12], Primož Vavpetič[11], Primož Pelicon[11], Philipp Kukura[9], Justin L. P. Benesch[9], Kenji Iwasaki[2,13] & Jonathan G. Heddle[1,3]*

Symmetrical protein cages have evolved to fulfil diverse roles in nature, including compartmentalization and cargo delivery[1], and have inspired synthetic biologists to create novel protein assemblies via the precise manipulation of protein–protein interfaces. Despite the impressive array of protein cages produced in the laboratory, the design of inducible assemblies remains challenging[2,3]. Here we demonstrate an ultra-stable artificial protein cage, the assembly and disassembly of which can be controlled by metal coordination at the protein–protein interfaces. The addition of a gold (I)-triphenylphosphine compound to a cysteine-substituted, 11-mer protein ring triggers supramolecular self-assembly, which generates monodisperse cage structures with masses greater than 2 MDa. The geometry of these structures is based on the Archimedean snub cube and is, to our knowledge, unprecedented. Cryo-electron microscopy confirms that the assemblies are held together by 120 S–Au^{I}–S staples between the protein oligomers, and exist in two chiral forms. The cage shows extreme chemical and thermal stability, yet it readily disassembles upon exposure to reducing agents. As well as gold, mercury(II) is also found to enable formation of the protein cage. This work establishes an approach for linking protein components into robust, higher-order structures, and expands the design space available for supramolecular assemblies to include previously unexplored geometries.

Successful strategies for the design of new protein cages make use of precisely oriented oligomeric protein fusions[4] or the computational design of novel protein–protein interfaces via the introduction of multiple hydrogen-bond and hydrophobic interactions[5]. However, one drawback of these methods is that the resulting assemblies are static; that is, their assembly and disassembly cannot be modulated using external stimuli, which is a desirable trait for smart nanomaterials. Metal-directed protein assembly presents an attractive alternative in this regard: inspired by supramolecular coordination chemistry[6], it involves directional metal ion coordination between protein surfaces as an alternative to protein–protein interactions, which greatly simplifies the design problem[7]. Although a wide variety of inducible metal-mediated protein oligomers and arrays have been successfully prepared in this manner[7–10], the generation of novel three-dimensional cage-like assemblies remains challenging; the closest example prepared so far is an engineered ferritin that can recover the native cage architecture upon Cu^{II} binding at interfacial sites[11].

Here we generate a protein cage for which assembly and disassembly can be triggered via metal ion coordination. In our previous work on TRAP (trp RNA-binding attenuation protein)—a bacterial ring-shaped protein[12] amenable to genetic modification[13–15]—we showed that a cysteine-substituted variant could form non-native shell architectures when reacted with triphenylphosphine-derivatized gold nanoparticles, through an unknown mechanism[16,17]. We proposed that metal ion–thiol interactions could be responsible for the formation of precise higher-order assemblies. To explore this idea, here we engineered a double-mutant TRAP bearing both a lysine-to-cysteine mutation at residue 35 (K35C), which generates 11 equally spaced thiol groups along the outer rim of the oligomeric ring, and an arginine-to-serine mutation at residue 64 (R64S), which neutralizes positive charges around the central cavity of the ring to prevent non-specific interactions with anionic groups[17] (TRAP(K35C/R64S); Fig. 1a). A minimal reaction containing purified TRAP(K35C/R64S) and monosulfonated chloro(triphenylphosphine)gold(I) (Au-TPPMS; Fig. 1b) as a source of Au^{I} ions resulted in the efficient self-assembly of monodisperse spheres ('TRAP-cage'), which were around 22 nm in diameter (Fig. 1c, d, Extended Data Fig. 1) and were visible within minutes. The optimum pH of the reaction was found to be 8 (Fig. 1e, Extended Data Fig. 1). Single-molecule mass photometry[18] enabled the kinetic tracking of TRAP-cage formation in situ after the addition of Au-TPPMS (Fig. 1e, Supplementary Videos 1–9). In the absence of Au-TPPMS, we found a homogeneous distribution of TRAP rings (Fig. 1e, inset). Upon the addition of Au-TPPMS, we observed the appearance of partially assembled TRAP-cages with an average mass of 1,080 kDa; these then transitioned towards fully assembled cages (2,160 kDa) with an exponential time constant of 351 ± 66 s.

The structure of the TRAP-cage was elucidated using cryo-electron microscopy single-particle analysis (Extended Data Figs. 2–4). An initial map (4.7 Å) showed a cage structure that lacked expected chiral features at the level of individual protein components (Extended Data Fig. 2). A second round of three-dimensional classification using finer angular sampling was then carried out; this yielded two unambiguous maps at 3.7 Å that displayed identical features but opposite chirality (Fig. 1f, Extended Data Figs. 2–4), with the left-handed and right-handed forms found in roughly equal populations based on particle counts (46.5% and 53.5%, respectively).

The maps revealed a spherical cage with unusual architecture, featuring 24 uniform rings and six square apertures along three orthogonal axes (Fig. 1f, g). The overall arrangement corresponds to a snub cube: an Archimedean solid with underlying octahedral (432) symmetry and an axial twist that imparts chirality (Fig. 1h). Each ring occupies an equivalent position on a snub cube vertex, bounded by

[1]Heddle Initiative Research Unit, RIKEN, Saitama, Japan. [2]Laboratory of Protein Synthesis and Expression, Institute for Protein Research, Osaka University, Osaka, Japan. [3]Bionanoscience and Biochemistry Laboratory, Malopolska Centre of Biotechnology, Jagiellonian University, Kraków, Poland. [4]Department of Cell Biology and Imaging, Institute of Zoology and Biomedical Research, Jagiellonian University, Kraków, Poland. [5]Postgraduate School of Molecular Medicine, Warsaw, Poland. [6]David R. Cheriton School of Computer Science, University of Waterloo, Waterloo, Ontario, Canada. [7]Faculty of Mathematics and Computer Science, Jagiellonian University, Kraków, Poland. [8]Department of Mathematical Sciences, Durham University, Durham, UK. [9]Department of Chemistry, Physical & Theoretical Chemistry Laboratory, University of Oxford, Oxford, UK. [10]Institute of Nuclear Physics, Polish Academy of Sciences, Kraków, Poland. [11]Jožef Stefan Institute, Ljubljana, Slovenia. [12]Jožef Stefan International Postgraduate School, Ljubljana, Slovenia. [13]Life Science Center for Survival Dynamics, Tsukuba Advanced Research Alliance (TARA), University of Tsukuba, Tsukuba, Japan. [14]Present address: Biomacromolecules Research Team, Center for Sustainable Resource Science, RIKEN, Saitama, Japan. [15]Present address: Department of Ecology and Evolution, University of Chicago, Chicago, IL, USA. *e-mail: jonathan.heddle@uj.edu.pl

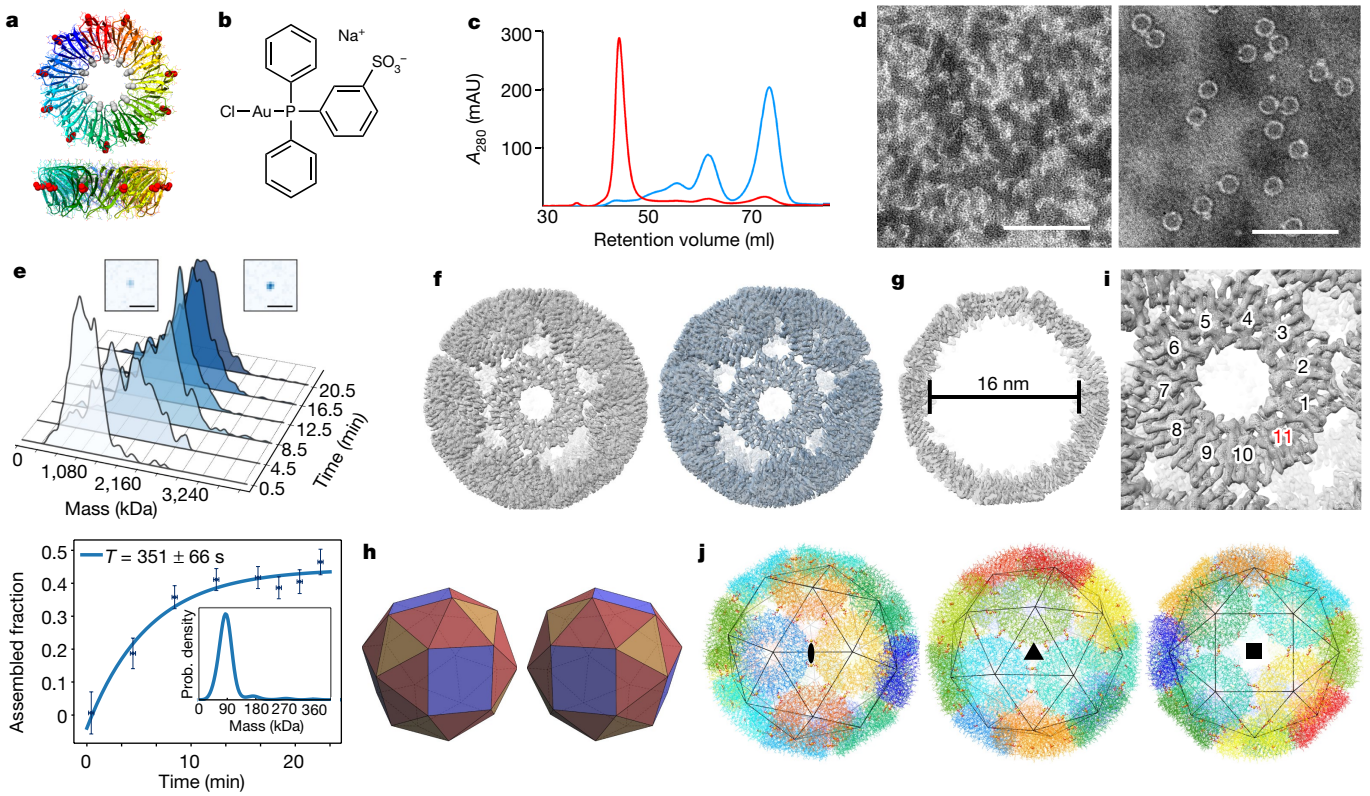

Fig. 1 | Formation of TRAP-cage. a, Structure of the TRAP(K35C/R64S) building block, shown in two orthogonal views (based on PDB ID: 4V4F). Substituted residues Cys35 and Ser64 are modelled as red and grey spheres, respectively. **b**, Chemical structure of Au-TPPMS. **c**, Results of size-exclusion chromatography, with 1 mM (monomer concentration) TRAP(K35C/R64S) before (blue) and 3 days after (red) reaction with Au-TPPMS. mAU, milli absorbance units. **d**, Transmission electron microscopy (TEM) images of unreacted TRAP(K35C/R64S) showing aggregates with no evidence of cage structures (left) and cages purified by size-exclusion chromatography after mixing TRAP(K35C/R64S) and Au-TPPMS (right). Scale bars, 100 nm. **e**, Top, monitoring TRAP-cage assembly with single-molecule mass photometry. The insets show representative single-particle images of partially (left) and fully assembled (right) cages. Scale bars, 1 μm. Bottom, extracted assembly kinetics. The horizontal error bars represent 15 s, as dictated by the length of a single measurement; the vertical error bars show the standard error on the area of Gaussian fit, calculated from the covariance matrix of the fit parameters. The inset shows results for TRAP(K35C/R64S) without addition of Au-TPPMS, exhibiting mostly monomeric TRAP (11-mer) rings (90 kDa), with weak signatures of small oligomeric assemblies thereof. **f**, Cryo-electron microscopy density maps of the left-handed and right-handed forms of TRAP-cage, refined to 3.7 Å resolution. **g**, Cutaway view of the left-handed map, showing a hollow interior. **h**, Snub cube (left-handed and right-handed forms) consisting of 32 regular triangles and 6 square faces. The four-, three- and two-fold rotational axes are represented in blue, yellow and red, respectively. **i**, Magnified view of the left-handed map showing 11-fold rotational symmetry of ring elements and prominent density bridges connecting adjacent rings. Positions 1–10 make contacts with neighbouring rings, whereas 11 is unattached and defines the side of a square aperture. **j**, Refined left-handed cage model, consisting of 24 TRAP(K35C/R64S) rings, with each ring positioned on the vertex of a snub cube (wire model). Three views are indicated, centred on the (from left to right) two-, three- and four-fold symmetry axes.

five neighbouring rings and a gap that defines one side of a square aperture. Crucially, all 24 rings preserved the 11-fold rotational symmetry (C_{11}) of native TRAP protein (Fig. 1i). Refinement of TRAP(K35C/R64S) models against each map produced excellent results (Extended Data Table 1). Overall, each chiral assembly is composed of 264 identical TRAP(K35C/R64S) subunits (Fig. 1j).

Closer examination showed that the ring densities are interconnected through staple-like bridges: there are two staples between each pair of neighbouring rings, totalling 120 staples per cage. In the refined models, ten Cys35 side chains of each TRAP(K35C/R64S) ring align with the staple positions, while the unlinked side chain of the 11th subunit points towards the four-fold aperture (Figs. 1i, 2a). We observed an enlargement at the midpoint of each staple density, which was interpreted as an Au^{I} ion coordinated between the two proximal thiol ligands with the preferred linear geometry[19] (Fig. 2a). No other ring–ring interactions were observed, apart from possible hydrogen bonding between the side chains of Asn18 and Asp37.

The presence of gold in the final structures was investigated using electrothermal atomic absorption spectroscopy (Extended Data Fig. 5a) and was quantified as 112 ± 8 Au atoms per assembly, in close agreement with the predicted value of 120. The presence of gold was corroborated by native mass spectrometry—which produced peaks that suggest stable S–Au^{I}–S linkages (Fig. 2b–d)—proton-induced X-ray emission, and X-ray photoelectron spectroscopy, whereas Raman spectroscopy showed no evidence of direct disulfide linkages (Extended Data Fig. 5b–i). The interactions between Au^{I} and Cys35 are expected to proceed through successive ligand displacement events involving Au-TPPMS, in agreement with Au^{I}–phosphine ligand-exchange hypotheses[20,21].

The metal-directed protein-assembly strategy predicts that a supramolecular complex of desired geometry can be generated by matching the inherent symmetry of a protein oligomer with the coordination geometry of an interacting metal ion[7]. To test this hypothesis in our context, we investigated other thiophilic transition metal ions (Au^{III}, Cu^{I}, Hg^{II} and Zn^{II}) for their ability to induce cage assembly upon reaction with TRAP(K35C/R64S) (Fig. 2e, f, Extended Data Fig. 6a–c). Whereas there was little or no evidence of cage structures upon the addition of Au^{III}, Cu^{I} and Zn^{II}, the addition of Hg^{II} triggered the formation of uniform cages that were indistinguishable from the gold-derived structures, consistent with the linear two-coordinate geometry[22] of mercury(II).

To test the robustness of the TRAP-cage geometry, we varied the position of the cysteine residues in the TRAP ring by using two additional surface mutants: TRAP(D15C), containing an aspartic

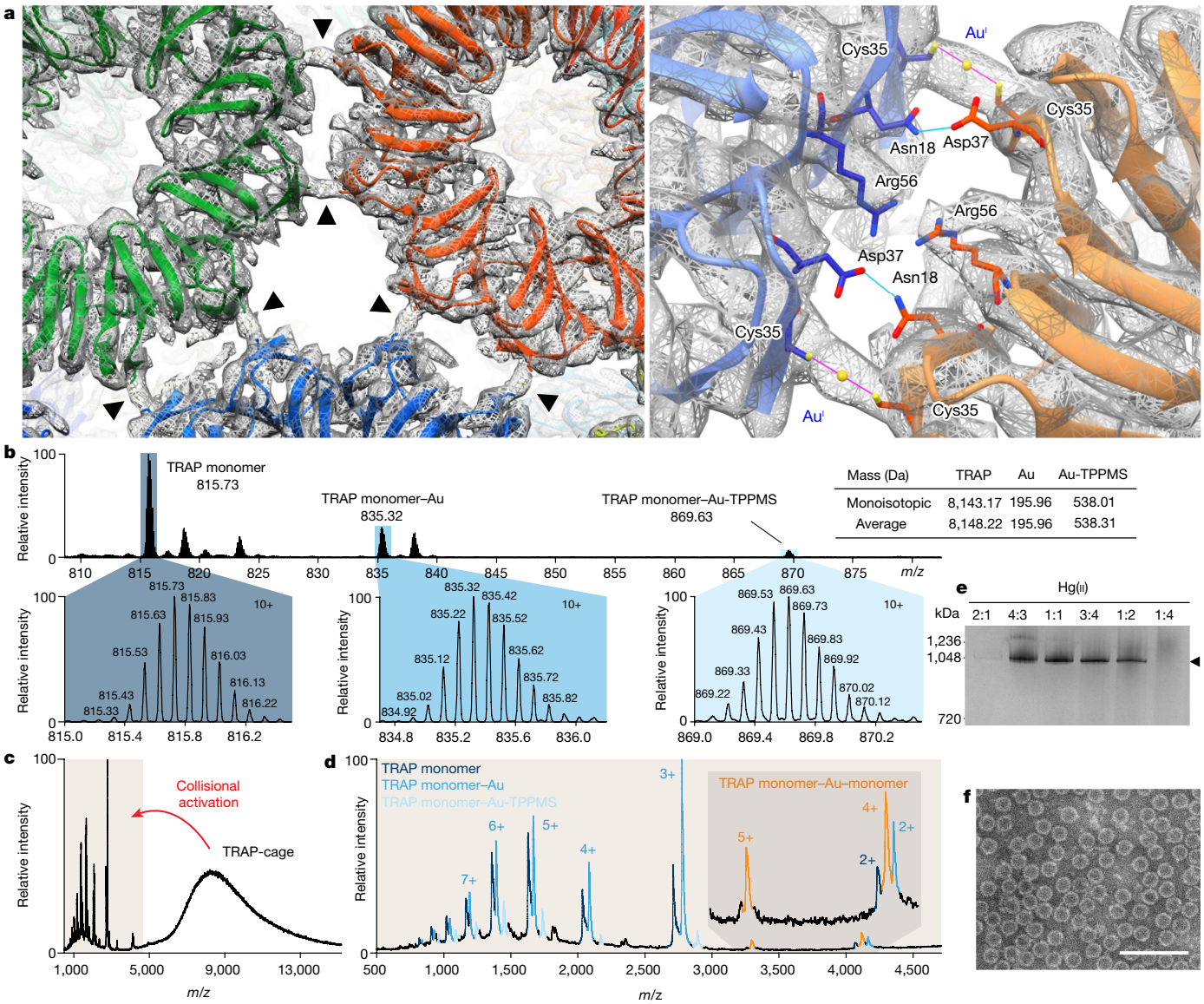

Fig. 2 | TRAP-cage is held together via Cys–Au^{I}–Cys coordination. **a**, Left, left-handed TRAP-cage model and map. The arrowheads indicate density bridges connecting neighbouring TRAP(K35C/R64S) rings. Right, close-up of the interface between two TRAP(K35C/R64S) rings. Individual Au^{I} ions are held in linear coordination between two Cys35 side chains from the neighbouring rings (magenta lines). No other intermolecular inter-ring interactions are apparent, except for possible hydrogen bonding between the side chains of Asn18 and Asp37 (light blue lines). **b**, Denaturing liquid chromatography–mass spectrometry data reveal three forms of TRAP monomer: unliganded protein (dark blue); monomer bound to a single gold atom (blue); and monomer bound to a gold atom and TPPMS ligand (light blue). Magnifications of the different peaks enable accurate-mass determination for unambiguous assignment. The other, minor peaks correspond to salt adducts and/or other charge states. The inset table provides a list of TRAP masses, and the mass additions expected owing to the different modifications. These correspond well to the masses measured, taking into account the 10 protons responsible for the 10+ charge state. **c**, Native mass spectrometry of intact TRAP-cages performed at high collisional activation reveals a broad, unresolved region of signal at high mass-to-charge ratio (m/z), and a series of peaks at low m/z, corresponding to the dissociation of intact cages and the release of cage fragments. **d**, Expansion of the low-m/z region in **c**, showing assignment of the various charge state series. Monomeric TRAP, in both modified and unmodified forms (blues, same colouring as **b**), are the major fragments observed. Inset, peaks that can be assigned unambiguously to a TRAP dimer containing a single gold atom are observed, which validates the TRAP–Au^{I}–TRAP linkage hypothesis. **e**, Native PAGE confirms TRAP-cage formation with mercury(II) nitrate. The arrowhead indicates the position of TRAP-cage formed with Au-TPPMS. The molar ratios of TRAP(K35C/R64S) monomer:Hg^{II} are shown above the gel. **f**, TEM image showing products of the reaction between TRAP(K35C/R64S) and mercury(II) nitrate. Scale bar, 100 nm. For gel source data, see Supplementary Fig. 1.

acid-to-cysteine mutation at position 15, and TRAP(S33C), containing a serine-to-cysteine mutation at position 33. TRAP(S33C) could assemble into cages in the presence of Au-TPPMS, whereas TRAP(D15C) could not; this highlights the importance of secondary interactions in influencing the resultant architectures (Extended Data Fig. 6d–f).

The stability of TRAP-cage was measured over a range of conditions (Fig. 3a–e, Extended Data Fig. 7). Extremely high stability was observed upon exposure to high temperatures, chaotropic agents and a wide range of pH conditions, which is consistent with the stabilizing effect of metal coordination[23,24]. Despite their extreme stability the cages were fully reversible, and broke apart in response to millimolar levels of reducing agents, probably via ligand displacement mechanisms[20]. We also observed that the reaction of TRAP(K35C/R64S) with triphenylphosphine-derivatized gold clusters produced a cage with a similar structure and stability (Extended Data Figs. 8, 9).

From a geometrical perspective the TRAP-cage architecture presents an apparent paradox, given that C_{11}-symmetric polygons (hendecagons) are excluded from assembling into regular convex polyhedra

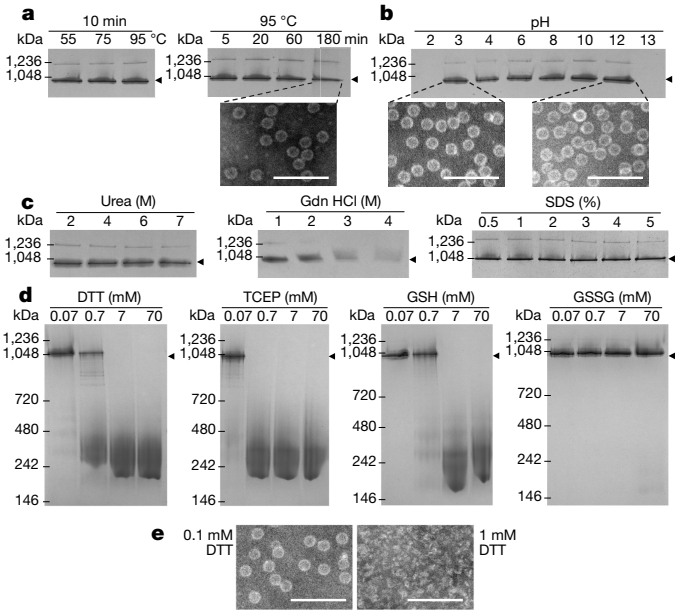

Fig. 3 | Extreme stability and controllable disassembly of TRAP-cage. **a**, The thermal stability of TRAP-cage. Native PAGE shows preservation of structural integrity at the indicated incubation times and temperatures. The TEM image was obtained after incubation at 95 °C for 180 min. **b**, Stability as a function of pH. No visible loss of structure was detected from pH 3–12 using native PAGE. TEM images were obtained after incubation at the indicated pH values. **c**, Effects of urea, guanidine hydrochloride (Gdn HCl) and SDS. **d**, Disassembly of TRAP-cage in the presence of reducing agents: dithiothreitol (DTT), tris(2-carboxyethyl) phosphine (TCEP), and reduced or oxidized glutathione (GSH and GSSG, respectively) at the indicated concentrations. **e**, TEM images show the structural integrity of TRAP-cage after treatment with DTT. Scale bars, 100 nm. On the gels, arrowheads indicate the position of TRAP-cage. For gel source data, see Supplementary Fig. 1.

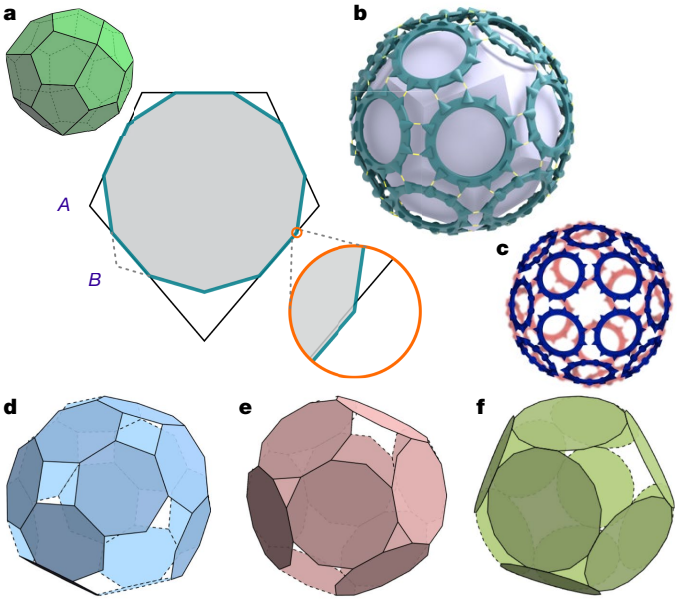

Fig. 4 | Unusual geometry of TRAP-cage. **a**, Top, pentagonal icositetrahedron, with 24 non-regular pentagonal faces. Bottom, a regular hendecagon can be placed at each face of the pentagonal icositetrahedron, such that five of the hendecagon's edges align almost perfectly with those of the pentagonal icositetrahedron. A magnified view shows that some hendecagon vertices lie very slightly outside of the pentagonal icositetrahedron face (others lie slightly inside). The near-coincidence arises because the obtuse angle $A \approx 114.81°$ of the pentagonal icositetrahedron face is almost equal to $B \approx 114.55°$ between non-consecutive hendecagon edges. **b**, Graphical representation showing the optimization of distances linking 24 regular 11-pointed rings (yellow). Translated to the scale of TRAP-cage, the results converge almost exactly to the ideal sulfur-to-sulfur distance of 4.7 Å. **c**, The 24 rings can be divided into two groups of 12, centred on opposite ends of a four-fold rotational axis of the TRAP-cage. One such group is coloured blue with the other group in red, faded in the background. Like the pentagonal icositetrahedron, the TRAP-cage as a whole is chiral. **d**–**f**, Examples of paradoxical cages that can be constructed from 7, 10 and 16-sided polygons. Deviations from ideality are expressed as relative deformations, termed rd_l and rd_a, and defined as the largest absolute value of the difference between the edge lengths and the average edge length, divided by the average value (rd_l), and similarly for the angles (rd_a). For comparison, rd_l and rd_a for TRAP-cage are 0.50% and 0.27%, respectively. **d**, A cage made out of 16 heptagons with 222 dihedral symmetry, derived by minimizing the energy of a mechanical model; $rd_l = 0.51\%$, $rd_a = 0.47\%$. **e**, A cage made out of 12 decagons obtained by dressing a cuboctahedron; $rd_l = 0.00\%$, $rd_a = 0.51\%$. **f**, A cage made out of 12 hexadecagons obtained by dressing a cuboctahedron; $rd_l = 0.00\%$, $rd_a = 0.64\%$.

(apart from prisms or antiprisms)[25]. To understand this, it is helpful to consider the geometric dual of the snub cube, the pentagonal icositetrahedron, which has 24 identical non-regular pentagonal faces and bears octahedral symmetry. We find that a regular hendecagon can be inscribed in each face of the pentagonal icositetrahedron, so that five of its edges nearly perfectly coincide with that of the irregular pentagon (Fig. 4a); this suggests a solid formed from 24 hendecagons, 56 triangles and 6 squares, which is mathematically impossible but is plausibly constructible as a physical object. To understand this geometry further, we modelled 24 copies of TRAP(K35C/R64S) oligomers as 11-pointed rings and optimized their positions in space to converge at a distance between two neighbouring points of 4.7 Å (the theoretical distance between two Cys-sulfur ligands in a S–Au^{I}–S linear complex). This simulation produced an arrangement similar to that of the TRAP-cage architecture (Fig. 4b, c); notably, the optimized S–S distances converged to the target with vanishingly small error, well within the physical tolerances required to form uniform protein cages from C_{11}-symmetric elements.

Our study supports the finding that a very small number of mutations can lead to profound changes in protein structural complexity via spontaneous self-assembly[26,27]. The architecture described by TRAP-cage has, to our knowledge, never been observed in nature, although a similar arrangement of 11-pointed stars appears in Islamic art[28]. Furthermore, our results suggest a possible avenue for building large capsid-like proteins using homomeric components. Viruses have achieved this by exploiting quasi-equivalent icosahedral symmetries to build shells of more than 60 subunits[29]; however, this poses an immense challenge for computationally designed cage systems, as it requires controlled switching between different oligomeric forms[30]. By contrast, TRAP-cage is a large, shell structure built from a single type of protein homo-oligomer, something that has been reported only rarely[27].

The general stability of TRAP-cage and its controllable disassembly hints at potential applications as an intracellular delivery agent. Finally, we suggest that there exists an entire domain of unexplored 'paradoxical geometries' beyond the unusual architecture embodied by TRAP-cage (Fig. 4d–f). Such geometries could be constructed using proteins or other biological molecules, and could potentially have unique properties.

Online content

Any methods, additional references, Nature Research reporting summaries, source data, statements of data availability and associated accession codes are available at https://doi.org/10.1038/s41586-019-1185-4.

Received: 4 June 2018; Accepted: 8 April 2019;
Published online: 08 May 2019

1. Aumiller, W. M., Uchida, M. & Douglas, T. Protein cage assembly across multiple length scales. *Chem. Soc. Rev.* **47**, 3433–3469 (2018).
2. Bale, J. B. et al. Accurate design of megadalton-scale two-component icosahedral protein complexes. *Science* **353**, 389–394 (2016).

3. Yeates, T. O. Geometric principles for designing highly symmetric self-assembling protein nanomaterials. *Annu. Rev. Biophys.* **46**, 23–42 (2017).
4. Padilla, J. E., Colovos, C. & Yeates, T. O. Nanohedra: using symmetry to design self assembling protein cages, layers, crystals, and filaments. *Proc. Natl Acad. Sci. USA* **98**, 2217–2221 (2001).
5. King, N. P. et al. Computational design of self-assembling protein nanomaterials with atomic level accuracy. *Science* **336**, 1171–1174 (2012).
6. Holliday, B. J. & Mirkin, C. A. Strategies for the construction of supramolecular compounds through coordination chemistry. *Angew. Chem. Int. Ed.* **40**, 2022–2043 (2001).
7. Salgado, E. N., Radford, R. J. & Tezcan, F. A. Metal-directed protein self-assembly. *Acc. Chem. Res.* **43**, 661–672 (2010).
8. Brodin, J. D. et al. Metal-directed, chemically tunable assembly of one-, two- and three-dimensional crystalline protein arrays. *Nat. Chem.* **4**, 375–382 (2012).
9. Der, B. S. et al. Metal-mediated affinity and orientation specificity in a computationally designed protein homodimer. *J. Am. Chem. Soc.* **134**, 375–385 (2012).
10. Zhang, W. et al. Self-assembly of glutathione S-transferase into nanowires. *Nanoscale* **4**, 5847–5851 (2012).
11. Huard, D. J. E., Kane, K. M. & Tezcan, F. A. Re-engineering protein interfaces yields copper-inducible ferritin cage assembly. *Nat. Chem. Biol.* **9**, 169–176 (2013).
12. Antson, A. A. et al. The structure of trp RNA-binding attenuation protein. *Nature* **374**, 693–700 (1995).
13. Heddle, J. G., Yokoyama, T., Yamashita, I., Park, S.-Y. & Tame, J. R. H. Rounding up: engineering 12-membered rings from the cyclic 11-mer TRAP. *Structure* **14**, 925–933 (2006).
14. Heddle, J. G. et al. Using the ring-shaped protein TRAP to capture and confine gold nanodots on a surface. *Small* **3**, 1950–1956 (2007).
15. Miranda, F. F. et al. A self-assembled protein nanotube with high aspect ratio. *Small* **5**, 2077–2084 (2009).
16. Malay, A. D. et al. Gold nanoparticle-induced formation of artificial protein capsids. *Nano Lett.* **12**, 2056–2059 (2012).
17. Imamura, M. et al. Probing structural dynamics of an artificial protein cage using high-speed atomic force microscopy. *Nano Lett.* **15**, 1331–1335 (2015).
18. Young, G. et al. Quantitative mass imaging of single biological macromolecules. *Science* **360**, 423–427 (2018).
19. Häkkinen, H. The gold–sulfur interface at the nanoscale. *Nat. Chem.* **4**, 443–455 (2012).
20. Bhabak, K. P., Bhuyan, B. J. & Mugesh, G. Bioinorganic and medicinal chemistry: aspects of gold(I)-protein complexes. *Dalton Trans.* **40**, 2099–2111 (2011).
21. Urig, S. et al. Undressing of phosphine gold(I) complexes as irreversible inhibitors of human disulfide reductases. *Angew. Chem. Int. Ed.* **45**, 1881–1886 (2006).
22. Rulíšek, L. & Vondrásek, J. Coordination geometries of selected transition metal ions (Co^{2+}, Ni^{2+}, Cu^{2+}, Zn^{2+}, Cd^{2+}, and Hg^{2+}) in metalloproteins. *J. Inorg. Biochem.* **71**, 115–127 (1998).
23. Arnold, F. H. & Zhang, J. H. Metal-mediated protein stabilization. *Trends Biotechnol.* **12**, 189–192 (1994).
24. Brodin, J. D., Carr, J. R., Sontz, P. A. & Tezcan, F. A. Exceptionally stable, redox-active supramolecular protein assemblies with emergent properties. *Proc. Natl Acad. Sci. USA* **111**, 2897–2902 (2014).
25. Grünbaum, B. & Johnson, N. W. The faces of a regular-faced polyhedron. *J. Lond. Math. Soc.* **s1-40**, 577–586 (1965).
26. Garcia-Seisdedos, H., Empereur-Mot, C., Elad, N. & Levy, E. D. Proteins evolve on the edge of supramolecular self-assembly. *Nature* **548**, 244–247 (2017).
27. Sasaki, E. et al. Structure and assembly of scalable porous protein cages. *Nat. Commun.* **8**, 14663 (2017).
28. Huylebrouck, D. & Redondo, A. The Hendecagonal Stars in the Alhambra. In *Proc. Bridges Finland 2016* (eds Torrence, E. et al.) 497–500 (Tessellations, Phoenix, 2016).
29. Caspar, D. L. D. & Klug, A. Physical principles in the construction of regular viruses. *Cold Spring Harb. Symp. Quant. Biol.* **27**, 1–24 (1962).
30. Prasad, B. V. & Schmid, M. F. Principles of virus structural organization. *Adv. Exp. Med. Biol.* **726**, 17–47 (2012).

Acknowledgements We thank M. Michalak and R. Pałka for initial TRAP protein production, P. Afonine for assistance with PHENIX real space refinement, M. Kobiałka and O. Woźnicka for TEM imaging, A. Telk and D. Dudek-Adamska for electrothermal atomic absorption spectroscopy experiments and evaluation (with financial support no. POIG.02.02.00-12-023/08), and A. Naskalska for additional experiments. This work was performed in part under the International Cooperative Research Program of the Institute for Protein Research, Osaka University CEMCR-17-05. A.D.M. and J.G.H. were funded by RIKEN Initiative Research Funding awarded to J.G.H. A.D.M. was supported by a Kakenhi Grant-In-Aid for Challenging Exploratory Research (JSPS), no. 2556023. J.G.H., A.B., I.S., A.K. and K.M. were funded by the National Science Centre (NCN, Poland) grant no. 2016/20/W/NZ1/00095 (Symfonia-4). Raman spectroscopy experiments were performed using equipment purchased as part of a project co-funded by the Malopolska Regional Operational Program Measure 5.1 Krakow Metropolitan Area as an important hub of the European Research Area for 2007-2013, project no. MRPO.05.01.00-12-013/15. J.L.P.B. acknowledges support from the EPSRC EP/J01835X/1. T.P.W. was supported under grant no. Homing/2016-2/20. A.F., M.S.K. and P.K. were supported by a ERC starting investigator grant (337757). K.I. was supported by the Platform Project for Supporting Drug Discovery and Life Science Research (Basis for Supporting Innovative Drug Discovery and Life Science Research) from the Japan Agency for Medical Research and Development (AMED). Work at JSI was supported by Slovenian research agency grants nos P1-0112, I0-0005, J7-9398 and EU projects no. 227012 “SPIRIT” and no. 824096 “RADIATE”.

Reviewer information *Nature* thanks Jeroen Cornelissen, Todd Yeates and the other anonymous reviewer(s) for their contribution to the peer review of this work.

Author contributions A.D.M. designed experiments, produced the protein cage, wrote the manuscript and carried out other experiments not listed. J.G.H. designed experiments, carried out TEM and wrote the manuscript. C.S.K. produced mathematical models of the TRAP-cage. A.K. and B.M.A.G.P. wrote the algorithm to predict paradoxical cage structures. A.B. and A.D.M. built the atomic models. N.M. and K.I. carried out cryo-electron microscopy experiments. G.K.A.H., D.W. and J.L.P.B. carried out mass spectrometry experiments. T.P.W. carried out Raman and X-ray photoelectron spectroscopy experiments. A.F., M.S.K., A.B. and P.K. designed, carried out and analysed the single-molecule mass photometry experiments. P.P., P.V. and M.K. executed micro-proton-induced X-ray emission analysis. S.C. and K.M. produced the protein cage, carried out stability tests and transmission electron microscopy sample preparation. I.S. carried out protein production and purification, dynamic light scattering measurements and preparation of samples for TEM. S.C. and A.B. carried out TEM. All authors contributed to writing the manuscript.

Competing interests A.D.M. and J.G.H. are named as inventors on a patent application related to the use of gold to cross-link cysteine residues aimed at protein assembly construction.

Additional information

Extended data is available for this paper at https://doi.org/10.1038/s41586-019-1185-4.
Supplementary information is available for this paper at https://doi.org/10.1038/s41586-019-1185-4.
Reprints and permissions information is available at http://www.nature.com/reprints.
Correspondence and requests for materials should be addressed to J.G.H.
Publisher’s note: Springer Nature remains neutral with regard to jurisdictional claims in published maps and institutional affiliations.

METHODS

No statistical methods were used to predetermine sample size. The experiments were not randomized and the investigators were not blinded to allocation during experiments and outcome assessment.

Gold compounds. Chloro[diphenyl(3-sulfonatophenyl)phosphine]gold(I) sodium salt hydrate (Au-TPPMS) was purchased from STREM Chemicals UK and reconstituted in water to 5 mM stock concentration or in 50 mM Tris-HCl, pH 7.9, 0.15 M NaCl to 10 mM stock concentration before use. The gold nanoparticle (GNP) used was a diphenyl(*m*-sulfonatophenyl)phosphine-gold nanocluster with a 1–3 nm core diameter (MDL number MFCD17018839) from STREM Chemicals UK.

Protein expression and purification. In a typical purification, *Escherichia coli* BL21(DE3) cells (Novagen) transformed with pET21b plasmid harbouring the TRAP(K35C/R64S) gene, or pET151/D-TOPO for genes encoding TRAPs with alternative cysteines S33C and D15C, were grown at 37 °C with shaking in 3 l of LB medium with 100 μg ml^{-1} ampicillin until an optical density at 600 nm (OD_{600}) of 0.6 was reached, induced with 0.5 mM IPTG then further shaken for 4–5 h. Cells were collected by centrifugation and the pellet kept at −80 °C until use. Cells were lysed by sonication at 4 °C in 50 ml of 50 mM Tris-HCl, pH 7.9 or 8.5, 0.05 M NaCl in the presence of proteinase inhibitors (Thermo Scientific) and in the presence or absence of 2 mM DTT, and lysates were centrifuged at 66,063*g* for 0.5 h at 4 °C. The supernatant fraction was heated at 70 °C for 10 min, cooled to 4 °C, and centrifuged again at 66,063*g* for 0.5 h at 4 °C. The supernatant fraction was purified by ion-exchange chromatography on an ÄKTA purifier (GE Healthcare Life Sciences) using 4 × 5 ml HiTrap QFF columns with binding in 50 mM Tris-HCl, pH 7.9 or 8.5, 0.05 M NaCl, ±2 mM DTT buffer and eluting with a 0.05–1 M NaCl gradient. Fractions containing TRAP were pooled and concentrated using Amicon Ultra 10 kDa MWCO centrifugal filter units (Millipore) and the sample subjected to size-exclusion chromatography (SEC) on a HiLoad 26/600 Superdex 200pg column in 50 mM Tris-HCl, pH 7.9, 0.15 M NaCl ('cage buffer') at room temperature. Protein concentrations were calculated using the BCA protein assay kit (Pierce Biotechnology). SEC experiments shown are representative of experiments repeated at least once each giving similar results.

Cage assembly. Formation of TRAP-cage was carried out by mixing purified TRAP(K35C/R64S) and Au-TPPMS in aqueous solution. The typical 'standard cage formation conditions' consisted of equimolar amounts of TRAP(K35C/R64S) monomer and Au-TPPMS in cage buffer. The exact concentrations of reactants were tailored for each reaction but were typically as follows: 1 mM TRAP(K35C/R64S) (8.3 mg ml^{-1}) and 1 mM Au-TPPMS. Reactions were incubated for at least 3 days at room temperature; reaction times of up to three months were also found to give similar results. Formation of TRAP-cage was confirmed using TEM and native PAGE. Any precipitated material (aggregated protein, present in older samples) was removed by centrifugation at 12,045*g* for 5 min, and TRAP-cage was purified by SEC on either Superose 6 Increase 10/300 GL or HiPrep 16/60 Sephacryl S-500 HR columns or HiLoad 16/600 Superdex 200pg columns (GE Healthcare). Typically, unreacted TRAP(K35C/R64S) shows a heterogeneous size distribution, with a major peak corresponding to lower-molecular-weight TRAP ring assemblies and a smaller peak(s) corresponding to larger aggregates, probably resulting from disulfide-bond formation. Fractions containing the cage protein were pooled, concentrated using Amicon Ultra 0.5 100-kDa MWCO centrifugal filter units, and protein concentration was measured using the BCA protein assay (Pierce Biotechnology). The yield was calculated by passing TRAP(K35C/R64S), after the cage-forming reaction with Au-TPPMS, down a Superose 6 Increase column (GE Healthcare). Fractions containing TRAP-cage were collected and their purity confirmed by native PAGE. The concentration of the purified cage was determined by measuring absorbance at 280 nm compared to total protein concentration in the starting solution.

For formation of TRAP-cage using GNPs in place of Au-TPPMS, conditions used were similar to the conditions described above: in brief, purified TRAP(K35C/R64S) (final concentration of around 500 μM TRAP monomer) was mixed with GNP (final concentration approximately 500 μM) at room temperature in buffer containing 20 mM Tris-HCl, pH 8.0 and 0.15 M NaCl.

For testing the ability of other metals to support cage formation, mercury(II) nitrate (Merck), copper(I) iodide (Sigma-Aldrich), zinc(II) chloride (VWR Chemicals) and gold(III) chloride trihydrate (Sigma-Aldrich) were reconstituted in cage buffer to 5 mM stock concentration before use. TRAP(K35C/R64S) samples (0.8 mg ml^{-1} final concentration) were incubated for 3 days with varying metal ion concentrations. Results were monitored using native PAGE. Cages made using mercury(II) nitrate were imaged in TEM without further purification.

For testing the effect of pH on cage assembly, Au-TPPMS stocks were prepared as described above in 50 mM sodium acetate at pH 5.0, 50 mM potassium phosphate at pH 6.0 or 7.0, 50 mM Tris-HCl at pH 8.0 and 50 mM glycine-NaOH at pH 9.0.

For testing TRAP-cage formation at different pH values at different time points, reactions were carried out as described above for testing pH at a single time point with samples removed at the indicated times before mixing with 4× Native-PAGE sample buffer.

Cage stability. All agents used for cage-stability tests (DTT, TCEP, GSH, GSSG, SDS, Gdn HCl, urea) were reconstituted in water or cage buffer and the pH was adjusted when needed. Buffers used for pH stability tests were: 50 mM glycine-HCl at pH 2.0 or 3.0, 50 mM sodium acetate at pH 4.0, 50 mM potassium phosphate at pH 6.0, 50 mM Tris-HCl at pH 8.0, 50 mM glycine-NaOH at pH 10, 50 mM potassium phosphate at pH 12, 50 mM potassium chloride-NaOH at pH 13. Each sample was briefly centrifuged in a desktop centrifuge and a portion of supernatant removed and mixed with 4× native PAGE sample buffer and subjected to blue native PAGE. Cage-stability experiments were repeated at least once, each giving similar results.

Dynamic light scattering. Dynamic light scattering was carried out using a Zetasizer Nano ZS (Malvern). TRAP-cage samples were diluted to 0.2–0.4 μM cage in 50 mM Tris-HCl, 150 mM NaCl, pH 7.9 and centrifuged for 2 min at 12,045*g*. Each sample (50 μl) was analysed in a quartz cuvette (ZEN 2112) and preincubated for 120 s at 25 °C. The samples were measured with standard settings for 50 mM Tris-HCl, 0.15 M NaCl buffer. Results were given as volume distributions. Three TRAP-cage samples were measured, with each measurement repeated at least three times. All measurements gave highly similar results.

Single-molecule mass photometry. The experimental setup was identical to that described in a previous study[18], except for the use of a 633 nm laser diode (Lasertack). In brief, the collimated laser output is passed through two acousto-optic deflectors (AA Opto Electronic, DT SXY-400) mounted orthogonally to each other. The beam deflection is imaged into the back focal plane of a microscope objective (Olympus, 1.45 NA, 60×) by a 4f telecentric lens system after first passing through a polarizing beam splitter and a quarter-wave-plate. The light reflected at the glass–water interface together with that backscattered by the sample is collected by the objective, and this is separated from the incident light by the combination of the polarizing beam splitter and quarter-wave-plate. The reflected light is then selectively attenuated with respect to the scattering signal, by reimaging the back focal plane of the microscope objective onto a partially reflective mirror, as described previously[31]. The sample is then imaged onto a CMOS camera (Point Grey GS3-U3-23S6M-C) with 291.7× magnification, giving a pixel size of 20 nm per pixel. The focus position is maintained throughout the experiment by an active feedback loop using a totally internally reflected beam.

Data acquisition and analysis. The camera was run at 1 kHz and the recorded images were time-averaged twofold and pixel-binned 5 × 5 before saving. This gives an effective frame rate of 500 Hz and pixel size of 100 nm. At this imaging speed, the sensitivity was insufficient to detect individual 90-kDa subunits, producing a cut-off at 200 kDa for the smallest detectable objects. For control experiments to detect individual TRAP rings, data were recorded in a similar manner but were time-averaged down to 10 Hz in order to increase sensitivity and detect the 90-kDa rings. To reduce the number of binding events per second, the control data was measured at 100 nM.

A sample of TRAP(K35C/R64S) protein in cage buffer and Au-TPPMS was reacted at room temperature in a 1:1 ratio at 100 μM each. At various time points, beginning 30 s after mixing the two components, 5 μl of the mixture was diluted to 10 μM and immediately added to a well of a silicon gasket (3 mm diameter, 1 mm thickness) fixed to a microscope coverslip (#1.5, 24 mm × 52 mm, Menzel Glazer) already containing 15 ul of cage buffer and mixed with the volume of the 5 μl micro-pipette. Fifteen seconds after addition of sample to the well, the acquisition software was triggered and the sample was measured for 30 s.

Image analysis was performed using the method described previously[18] to extract the masses of the observed particles. Kernel density estimates for each time point were generated using a Gaussian kernel with a bandwidth of 40 kDa. To determine the proportion of formed cage with time, a Gaussian constrained to the expected mass of the cage and width for a single species of that mass ($\mu = 2{,}160$ kDa, $\sigma = 110$ kDa) was fit to a normalized histogram of each time point and the area taken. The σ value was chosen through extrapolation of values for known calibrants.

The resulting plot of proportion of cage against time was fit to a global association rate fit:

$$f(x) = k(1-e^{-x/\tau})$$

where k is the maximum proportion of cage and τ is the formation time. Single-molecule mass photometry experiments were run twice using different dilutions of the same protein sample, giving similar results.

Three-dimensional reconstruction of the initial cryo-electron microscopy structure of TRAP-cage. A few microlitres of purified TRAP-cage formed using GNPs in 20 mM Tris-HCl, pH 8.0, 0.15 M NaCl were applied onto glow-discharged C-flat grids (1 μm hole, 1 μm space, 400 mesh copper grids) in the humidity-controlled chamber of an EM GP (Leica Microsystems) followed by blotting and plunge freezing. Cryo-electron microscopy (cryo-EM) images were collected at

liquid-nitrogen temperature on a JEM-2200FS transmission electron microscope (JEOL) operated at 200 kV using a CT3500 cryo-transfer holder (Gatan). Images were recorded using a K2 summit direct electron camera (Gatan) using super-resolution counting mode. A nominal magnification of 20,000× reading in the electron microscope used for image recording corresponds to a calibrated super resolution pixel size of 1.01 Å per pixel on the specimen. Dose fractionation mode was used, setting the frame exposure time to 0.2 s and the total exposure time to 5 s. The dose rate on the camera was set to be less than 2 counts per sub-pixel per second. Stacked images obtained by dose-fractionation mode underwent motion correction using software as described previously[32]. All of the 25 frames in each stacked image were used to calculate a sum of frames after motion correction. Each summed image was 2 × 2 binned, which were used for the following image processing. The phase of the cryo-EM images was corrected using ctfDisplay and mrcImageCTFCompensation implemented under EOS[33]. Boxing 4,472 particles from the phase-corrected images was done using EMAN2[34]. A first three-dimensional (3D) model was obtained at 18 Å (Fourier shell correlation (FSC) = 0.5) using EMAN1.9[35]. This was used as a reference model for the image analysis by RELION 1.3 and 1.4[36]. The 3D map of 16.5 Å resolution, obtained without any symmetrical operation after using 3D auto-refine in RELION, was used for the following high-resolution work as an initial model.

Cryo-EM single-particle reconstruction of TRAP-cage formed using GNPs at higher resolution. A purified sample formed using GNPs (3 μl of 0.13 mg ml^{-1}) was applied to glow-discharged holey carbon grids (Quantifoil R 1.2/1.3, Mo 200 mesh) with a thin amorphous carbon film of about 10 nm thickness over the holes and incubated for 30 s at 4 °C and 100% humidity. Grids were then blotted for 3.0 s and plunged into liquid ethane using a Vitrobot Mark IV (FEI). Data were recorded semi-automatically using the EPU software on a transmission electron cryo-microscope (FEI Titan Krios) operated at an accelerating voltage of 300 kV and at a nominal magnification of 75,000×. Images (0.91 Å per pixel) were recorded at applied underfocus values ranging from approximately −1.0 to −3.0 μm on a Falcon II direct electron detector (FEI) as 16 frames in 1.0 s exposure with a total electron dose of 20 electrons per Å^2. Data were subsequently aligned and summed using MotionCor2[37] to obtain a final dose-weighted image and then 2× binning was performed using the Bsoft program package[38], resulting in a pixel size of 1.82 Å for further image processing. Estimation of the contrast-transfer function was performed using CTFFIND4[39]. Micrographs exhibiting poor power spectra based on the extent and regularity of the Thon rings were rejected. Initially, approximately 2,000 particles were manually picked from 43 micrographs and subjected to reference-free two-dimensional (2D) classification using EMAN 2.1[34]. Ten representative 2D class averages were selected as templates for automated particle picking using Gautomatch (http://www.mrc-lmb.cam.ac.uk/kzhang/). All subsequent processing steps were performed in RELION 2.0[36]. A total of 131,812 auto-picked particles from 2,637 micrographs were subjected to reference-free 2D classification to remove aberrant particles. Particles in 22 representative classes showing spherical shapes were selected (58,157 particles) for the following processes. The selected particles were subjected to 3D structure refinement and post-processing without any symmetry (C1 symmetry), where the initial low-resolution structure as described above was used for the reference in the 3D classification after low-pass filtering to 60 Å. The resolution was estimated to 5.6 Å by the gold-standard Fourier shell correlation (FSC = 0.143 criterion), after applying a soft spherical mask on the two reconstructions refined from half of the datasets independently. Further structural analysis was carried out using TRAP-cage formed using Au-TPPMS rather than GNPs.

Cryo-EM single-particle reconstruction of TRAP-cage formed using Au-TPPMS. A purified sample (3 μl of 0.89 mg ml^{-1}) formed using Au-TPPMS was applied to glow-discharged holey carbon grids (Quantifoil R 1.2/1.3, Mo 200 mesh) with a thin amorphous carbon film of around 10 nm thickness over the holes and incubated for 30 s at 4 °C and 100% humidity. Grids were then blotted for 3.0 s and plunged into liquid ethane using a Vitrobot Mark IV (FEI). Data were recorded semi-automatically using the EPU software on a transmission electron cryo-microscope (FEI Titan Krios) operated at an accelerating voltage of 300 kV and at a nominal magnification of 75,000×. Images (0.91 Å per pixel) were recorded at applied underfocus values ranging from approximately −0.9 to −3.4 μm on a Falcon II direct electron detector (FEI) as 32 frames in 2.0-s exposure with a total electron dose of 40 electrons per Å^2. Data were subsequently aligned and summed using MotionCor2[37] to obtain a final dose-weighted image and then 2× binning was performed using the Bsoft program package[38], resulting in a pixel size of 1.82 Å for further image processing. Estimation of the contrast transfer function was performed using CTFFIND4[39]. Micrographs exhibiting poor power spectra based on the extent and regularity of the Thon rings were rejected (96 micrographs). Initially, approximately 2,000 particles were manually picked and subjected to reference-free 2D classification using EMAN 2.1[34]. Ten representative 2D class averages were selected as templates for automated particle picking using Gautomatch (http://www.mrc-lmb.cam.ac.uk/kzhang/). All subsequent processing steps were performed in RELION 2.0[36]. A total of 1,085,623 auto-picked particles from 10,290 micrographs were subjected to reference-free 2D classification to remove aberrant particles. Particles in 5 representative classes showing spherical shapes were selected (578,865 particles) for the following processes. The selected particles were subjected to 3D classification into three classes using an angular sampling of 3.7° for 25 iterations without any symmetry (C1 symmetry), where the initial low-resolution structure as described above was used for the reference in the 3D classification after low-pass filtering to 60 Å. The particles (176,463 particles) in a class showing the most symmetrical cage structure with regular density distribution were selected for the following processes. However, although the density map clearly showed the overall TRAP-cage structure as a sphere with twenty-four 11-membered rings, the structure at the level of the individual rings was devoid of protein chiral features and showed mixed features of two mirrored protein structures, contrary to expectations from the protein structure previously determined by X-ray crystallography[40], which is suggestive of the existence of chiral cage structures. Therefore, we performed a second round of 3D classification using a finer angular sampling of 1.8° for 25 iterations, without any symmetry, which produced two maps displaying alternative chiral arrangement of ring elements. Each structure (class I: 94,338 particles and class II: 82,125 particles) was refined individually with the C1 (asymmetric reconstruction), C4 and D4 symmetries. The resolutions of the class I were estimated as 3.7 (octahedral symmetry), 3.9 (D4), 4.1 (C4), and 4.4 Å (C1) and the resolutions of the class II were estimated to 3.9 (D4 sym.), 4.2 (C4 sym.), and 4.5 Å (C1 sym.) by the gold-standard Fourier shell correlation (FSC = 0.143 criterion), after applying a soft spherical mask on the two reconstructions refined from the half of the datasets independently. The maps of class I and II with octahedral symmetry were sharpened with B-factors of −236 and −244 Å^2, respectively. Local resolution was estimated using ResMap[41]. Figures were prepared using UCSF Chimera[42].

Structural refinement. The initial atomic coordinate model was based on the TRAP crystal structure (PDB: 4V4F[40]), with the Cys35 and Ser64 substitutions modelled in Coot[43] to generate TRAP(K35C/R64S) ring structures. Note that residue positions have been renumbered from the initial deposited PDB to reflect the actual positions in the coding sequence of TRAP from *Geobacillus stearothermophilus* (for example, the mutated Lys-to-Cys residue was assigned to residue number 37 in the original PDB file 4V4F but corresponds to residue number 35 in our analyses). Initial inspection of the density maps revealed areas of weak or missing density, and thus the structure of each TRAP subunit was truncated to residues 6–72; in addition residues 22–32 (corresponding to a loop that exhibits high flexibility in the apo-form of TRAP[44]) were omitted from the model to reflect this. Refinement of the left-handed and right-handed structures followed a similar regime. Twenty-four copies of TRAP(K35C/R64S) rings were initially fit into the cage density by rigid-body refinement using Phenix real-space refinement[45]. Optimization of the original cryo-EM map voxel size using the high-resolution TRAP crystal structure[40] as a reference was performed as follows, in a manner analogous to that of previous reports[46,47]. Comparison of cross-correlation scores of the fits between a simulated map of the TRAP(K35C/R64S) ring atomic model and the cryo-EM map at varying voxel scales (starting from the original 1.82 Å per voxel and varying by 0.01 increments) was performed using Chimera, with the optimal results corresponding to a map scale of 1.74 Å per voxel. Similar results were obtained by performing rigid-body refinement of individual subunits of 24 TRAP(K35C/R64S) rings onto the cryo-EM density at varying scales using Phenix[45]. Au^{I} atoms (120 in total) were docked manually into the prominent density between the Cys35 side chains from neighbouring rings of the rigid-body fitted model, and subsequently 15 macro cycles of Phenix real-space refinement were run using the 1.74 Å-per-voxel map, including rigid-body refinement, global minimization, a single round of simulated annealing, and adp refinement; restraints on the Au–S bond lengths and S–Au–S bond angles were applied during the later stages of refinement. Validation of the refined models was carried out using MolProbity[48]. Analysis of interfacial contacts in the TRAP-cage models was performed using PDBePISA (http://www.ebi.ac.uk/pdbe/pisa/)[49].

Transmission electron microscopy. Samples were typically diluted to a final protein concentration of 0.025 mg ml^{-1}, centrifuged briefly in a desktop centrifuge and the supernatant applied onto hydrophilized carbon-coated copper grids (STEM), negatively stained with 3% phosphotungstic acid, pH 8, and visualized using a JEOL JEM-1230 80 kV instrument. All TEM results shown were repeated at least once, independently, each giving similar results.

Native PAGE. Samples were run on 3–12% native Bis-Tris gels following the manufacturer's recommendations (Life Technologies). Samples were mixed with 4× native PAGE sample buffer (200 mM BisTris, pH 7.2, 40% w/v glycerol, 0.015% w/v bromophenol blue). As a qualitative guide to the molecular weights of migrated bands, NativeMark unstained protein standard (Life Technologies) was used. Where blue native PAGE was performed, protein bands were visualized according to the manufacturer's protocol (Life Technologies), otherwise InstantBlue protein stain (Expedeon) was used. All native PAGE gels were repeated independently at least once with each repeat giving similar results.

Electrothermal atomic absorption spectrometry. A sample mass of 2 mg was dissolved in 25 ml with 0.2% HCl. The solution was then diluted 25 times before determination of total gold was performed using an electrothermal atomic absorption spectrometer (PinAAcle 900Z, Perkin Elmer), with Zeeman background correction, at a wavelength of 242.80 nm (slit width of 0.7 nm). The measured volume of the sample solution was 10 μl and to each sample a mixture of matrix modifiers (5 μg of $Pd(NO_3)_2$ and 3 μg of $Mg(NO_3)_2$) was added. Five sets of measurements were carried out for each sample, with each set consisting of three repeats.

Proton-induced X-ray emission. The S:Au ratio was determined using micro-proton-induced X-ray emission (micro-PIXE) measurements performed with a high-energy focused proton beam (nuclear microprobe) in the tandem accelerator laboratory of the Jožef Stefan Institute[50]. The beam is focused by a magnetic quadrupole triplet lens and scanned over the square-shaped area of interest by magnetic deflectors. The micro-PIXE setup is described in detail in a previous study[51]. X-ray analysis was carried out by a Peltier-cooled silicon drift detector, equipped with ultra-thin vacuum window and aluminium-coated 1-μm-thick Mylar foil to block visible-light photons.

Standard sample substrate for micro-PIXE analysis was used for the protein analysis, consisting of a 100-nm-thick Pioloform foil spanned over a 0.5-mm-thick aluminium frame with 8 mm aperture. TRAP (approximately 0.5 mg ml^{-1}) was applied to the centre of the aperture as two consecutive depositions of 0.5 μl and dried. The second deposition took place after complete drying of the first. The sample was mounted on the sample holder and inserted into the high-vacuum system with a vacuum of 2×10^{-7} mbar. We applied a 3-MeV beam with a diameter of 1.0 μm and beam current of 200 pA. The transmitted proton beam was detected with a dedicated beam stopper incorporating an on–off axis detector for scanning transmission ion microscopy (on–off axis STIM[52]) providing the information on the sample thickness. The beam was scanned across the selected field of interest, varying from a maximum scanning field of 2,000 × 2,000 μm^2 down to 400 × 400 μm^2. All the measurements were taken in the listmode, which enables data sequence recovery and monitoring of eventual sample evolution during the measurements. The methodology of the micro-PIXE protein analysis was adopted according to published methods[53]. Quantification was carried out considering that the TRAP-cage structural model has a bridging gold atom between 10 of the 11 Cys35 residues of each TRAP ring. Given the presence of an additional sulfur atom per TRAP monomer (from methionine) this would give a ratio of S:Au of 4.4:1 assuming that the Cys35 at the 11th monomer of each ring did not bind a gold or 3.7:1 assuming that it did. The samples were treated as samples of finite thickness, and proton beam stopping as well as X-ray attenuation in the sample were taken into account within the Gupixwin program[54]. The precision of the method was validated during each set of experiments by measurement of reference pure metals Al, Ti, Cu and Au, Standard Reference Material of the National Institute for Standards and Technology (NIST) Naval Brass (C1107) and a set of thin evaporated X-ray fluorescence reference samples of Au and CuS_x produced by Micromatter.

X-ray photoelectron spectroscopy. X-ray photoelectron spectroscopy (XPS) analysis was performed on a VersaProbeII PHI scanning XPS spectrometer with Al Kα monochromatic X-ray (1,486.6 eV) excitation with a beam diameter of 100 μm on a 400 μm × 400 μm surface. The angle of the photoelectron analysis was 45° and the energy of electrons in the analyser was 46.95 eV. A dual neutralizer was applied on the test surface with the help of an Ar^+ ion beam with energy 7 eV and electrons with energy 1 eV. The XPS binding energies were calibrated using the carbon 284.80 eV 1*s* peak. The pressure inside the chamber was 4×10^{-9} mbar. Deconvolution and spectra analysis was done in the PHI MultiPak program (v.9.8.0.19).

Liquid–chromatography mass spectrometry. Purified TRAP-cage was denatured in 50 mM Tris-HCl buffer (pH 8.0) with 8 M urea at 56 °C for 30 min, then buffer-exchanged to 50 mM Tris-HCl buffer (pH 8.0) using a centrifugal filtration device (Amicon 3 kDa MWCO, Millipore). For denaturing liquid–chromatography mass spectrometry (LC–MS) analysis, the TRAP protein was desalted on a C18 pre-column (Acclaim PepMap100, C18, 300 μm × 1 cm; Thermo Scientific), then separated on a C18 column (Acclaim PepMap100, C18, 75 μm × 15 cm; Thermo Scientific) by a Dionex UltiMate 3000 RSLCnano System connected to a hybrid LTQ Orbitrap XL mass spectrometer (Thermo Scientific) via a dynamic nanospray source. A binary buffer system was used, with buffer A 0.1% formic acid in H_2O, and buffer B 0.1% formic acid in acetonitrile. The proteins were separated at 25 °C with a gradient of 1% to 90% buffer B at a flow rate of 300 nl min^{-1} over 60 min. The LTQ-Orbitrap XL was operated in positive ion mode with a nanoelectrospray voltage of 1.6 kV and capillary temperature of 275 °C. Survey full-scan MS spectra were acquired in the Orbitrap (*m/z* 300−4,000) with a resolution of 60,000. The data were processed using Xcalibur 2.2 (Thermo Scientific). For denaturing LC–MS, experiments were each repeated independently at least three times with representative results shown.

Native mass spectrometry. TRAP-cage samples at 0.8 mg ml^{-1} were prepared for native MS by buffer-exchanging into ammonium acetate (pH 6.9) using miniature spin columns (Micro Bio-Spin P-6, BioRad). This was performed in two steps: the first exchanged into 2.5 M ammonium acetate, the second into 200 mM ammonium acetate. Native MS experiments were performed using methods described previously[55], using a Q-ToF2 instruments (Waters), modified for the analysis of large protein ions[56]. Relevant instrument parameters were: nanoelectrospray capillary voltage, 1.9 kV; sample cone, 200 V; extractor cone, 10 V, acceleration into collision cell, 200 V. The collision cell was pressurized with argon at around 35 μbar. Data was calibrated externally using MassLynx software (Waters) and are shown without background subtraction and minimal smoothing. For native MS, experiments were each repeated independently at least three times with representative results shown.

Raman spectroscopy. Raman spectra were collected for TRAP-cage proteins in powder form and oxidized and reduced glutathione (Sigma) and for oxidized and reduced TRAP(K35C/R64S) rings. Spectra were collected using a Renishaw InVia Raman spectrometer equipped with a confocal microscope and CCD camera (1,024 × 256 pixels). The excitation wavelength was provided by a diode laser emitting at 532.0 nm. All spectra were acquired with a spectral resolution of 4 cm^{-1} in the spectral range of 100–3,200 cm^{-1} using 20× objective. The exposure time was 30 s with four acquisitions averaged to a single spectrum. The spectra were smoothed using a 13 points Savitzky-Golay filter, baselined using a rubber band algorithm and normalized to maximal intensity.

Mathematical modelling of TRAP-cage. We modelled the TRAP ring as a unit circle with 11 evenly spaced vertices on its perimeter. Assuming that the TRAP-cage has octahedral symmetry, then the complete cage can be assembled from this canonical ring by transformations about the 24 rotations in the octahedral group. The paradoxical cage in Fig. 4b suggests a set of 120 pairs of simulated S–Au–S bonds, one for each location where two hendecagonal vertices meet. For any given position and orientation of the canonical ring, the 24 rotated images in the simulated TRAP-cage will yield a set of 120 bond lengths. Our goal was to derive the six numbers defining the position and orientation of the canonical ring so that these 120 bonds are as close as possible in length to the ideal value of 4.7 Å. We can find a near-optimal position and orientation using numerical optimization, resulting in a configuration of TRAP rings, where the ideal value is matched to within an error of 5×10^{-9} Å, that is, essentially to within numerical accuracy and which is well within the physical tolerances for actual S–Au–S coordination bonds.

The optimal arrangement of TRAP rings was computed using a custom-written C++ program of about 1,000 lines of code. The core of the program uses the code for the 'downhill simplex' method of continuous simulated annealing, as provided in a previous publication[57]. The program also uses the Boost library (http://www.boost.org) for quaternions and random number generation. 3D visualizations were modelled and rendered in Rhinoceros 3D by Robert McNeel and Associates (http://www.rhino3d.com); the output from the optimizer was used to transform TRAP rings into position using a custom Python script.

Prediction of other paradoxical cages. To predict the geometry of other nearly regular cages, assemblies made of identical regular *n*-gons, for $n = 7, 8, \ldots, 17$ were considered. These polygonal faces were placed on the vertices of regular polyhedra so that the faces of the polyhedron correspond to the holes of the cage and the edges of the polyhedron to the links between adjacent faces of the cage. The polyhedra used for this 'dressing' method included all Platonic and Archimedean solids, prisms and antiprisms, ignoring those with faces having more than 6 edges. We wrote a computer program to construct many of the possible convex geometries from the method described above. The C++ program (of around 3,000 lines of code) outputs a file describing the topology—that is, the links between all the faces—for each potential cage thus found.

A second C++ program (about 8,400 lines of code) was then used to derive the geometric properties of the prospective cages. First, the polygonal faces were modelled as rigid bodies, with adjacent faces linked by two Hookean springs with a rest position set to 5% of the edge length. The energy of the system was then minimized using a Monte Carlo algorithm. The coordinates of the resulting polyhedron were then used by the program to model the cage as a set of rigid rods using an energy functional consisting of three terms: edge length deviations, face edge angular deviations, and degree of non-planarity. The first one measured by how much the edge lengths deviated from a chosen reference length. The second one measured by how much the angle between the face edges deviated from the angle of the regular polygon. The third term measured the level of non-planarity of the faces. Each term was multiplied by a weight factor, with the planarity weight set to three orders of magnitude larger than for the lengths and the angles. This enabled us to obtain structures with planar faces (with zero planarity distortions modulo numerical error). The energy functional was minimized using a Monte Carlo method, with the program generating a file containing the coordinates of each vertex, the topology of the cage, as well as the range of deformations

obtained for the angles and edge lengths. A detailed description of the algorithm will be given in a future publication.

Of the thousands of cages generated by the method described above, we selected candidates for which the level of deformation for both angles and edge lengths was smaller than 1%. In some cases—for example, the cage shown in Fig. 4d—the basic structure was obtained by manual construction of a physical model, with the topology then being fed into the second program for optimization.

Reporting summary. Further information on research design is available in the Nature Research Reporting Summary linked to this paper.

Data availability

The data that support the findings of this study are available from the corresponding author on reasonable request. The cryo-EM density maps have been deposited in the Electron Microscopy Data Bank under accession codes EMD-6966 (GNP-produced TRAP-cage), EMD-4443 (left-handed TRAP-cage) and EMD-4444 (right-handed TRAP-cage), and the coordinates have been deposited in the Protein Data Bank under accession numbers 6IB3 (left-handed TRAP-cage) and 6IB4 (right-handed TRAP-cage).

Code availability

Custom codes used to compute the optimal arrangement of TRAP rings and to predict paradoxical cages are available from the authors on reasonable request.

31. Cole, D., Young, G., Weigel, A., Sebesta, A. & Kukura, P. Label-free single-molecule imaging with numerical-aperture-shaped interferometric scattering microscopy. *ACS Photonics* **4**, 211–216 (2017).
32. Li, X. et al. Electron counting and beam-induced motion correction enable near-atomic-resolution single-particle cryo-EM. *Nat. Methods* **10**, 584–590 (2013).
33. Yasunaga, T. & Wakabayashi, T. Extensible and object-oriented system Eos supplies a new environment for image analysis of electron micrographs of macromolecules. *J. Struct. Biol.* **116**, 155–160 (1996).
34. Tang, G. et al. EMAN2: an extensible image processing suite for electron microscopy. *J. Struct. Biol.* **157**, 38–46 (2007).
35. Ludtke, S. J., Baldwin, P. R. & Chiu, W. EMAN: semiautomated software for high-resolution single-particle reconstructions. *J. Struct. Biol.* **128**, 82–97 (1999).
36. Scheres, S. H. RELION: implementation of a Bayesian approach to cryo-EM structure determination. *J. Struct. Biol.* **180**, 519–530 (2012).
37. Zheng, S. Q. et al. MotionCor2: anisotropic correction of beam-induced motion for improved cryo-electron microscopy. *Nat. Methods* **14**, 331–332 (2017).
38. Heymann, J. B. Bsoft: image and molecular processing in electron microscopy. *J. Struct. Biol.* **133**, 156–169 (2001).
39. Rohou, A. & Grigorieff, N. CTFFIND4: Fast and accurate defocus estimation from electron micrographs. *J. Struct. Biol.* **192**, 216–221 (2015).
40. Hopcroft, N. H. et al. The interaction of RNA with TRAP: the role of triplet repeats and separating spacer nucleotides. *J. Mol. Biol.* **338**, 43–53 (2004).
41. Kucukelbir, A., Sigworth, F. J. & Tagare, H. D. Quantifying the local resolution of cryo-EM density maps. *Nat. Methods* **11**, 63–65 (2014).
42. Pettersen, E. F. et al. UCSF Chimera—a visualization system for exploratory research and analysis. *J. Comput. Chem.* **25**, 1605–1612 (2004).
43. Emsley, P., Lohkamp, B., Scott, W. G. & Cowtan, K. Features and development of Coot. *Acta Crystallogr. D* **66**, 486–501 (2010).
44. Malay, A. D., Watanabe, M., Heddle, J. G. & Tame, J. R. H. Crystal structure of unliganded TRAP: implications for dynamic allostery. *Biochem. J.* **434**, 427–434 (2011).
45. Adams, P. D. et al. PHENIX: a comprehensive Python-based system for macromolecular structure solution. *Acta Crystallogr. D* **66**, 213–221 (2010).
46. Wang, Z. et al. An atomic model of brome mosaic virus using direct electron detection and real-space optimization. *Nat. Commun.* **5**, 4808 (2014).
47. Natchiar, S. K., Myasnikov, A. G., Kratzat, H., Hazemann, I. & Klaholz, B. P. Visualization of chemical modifications in the human 80S ribosome structure. *Nature* **551**, 472–477 (2017).
48. Chen, V. B. et al. MolProbity: all-atom structure validation for macromolecular crystallography. *Acta Crystallogr. D* **66**, 12–21 (2010).
49. Krissinel, E. & Henrick, K. Inference of macromolecular assemblies from crystalline state. *J. Mol. Biol.* **372**, 774–797 (2007).
50. Pelicon, P. et al. A high brightness proton injector for the Tandetron accelerator at Jožef Stefan Institute. *Nucl. Instrum. Methods Phys. Res. B* **332**, 229–233 (2014).
51. Vavpetič, P., Kelemen, M., Jenčič, B. & Pelicon, P. Nuclear microprobe performance in high-current proton beam mode for micro-PIXE. *Nucl. Instrum. Methods Phys. Res. B* **404**, 69–73 (2017).
52. Pallon, J. et al. An off-axis STIM procedure for precise mass determination and imaging. *Nucl. Instrum. Methods Phys. Res. B* **219–220**, 988–993 (2004).
53. Garman, E. F. & Grime, G. W. Elemental analysis of proteins by microPIXE. *Prog. Biophys. Mol. Biol.* **89**, 173–205 (2005).
54. Campbell, J. L., Hopman, T. L., Maxwell, J. A. & Nejedly, Z. The Guelph PIXE software package III: alternative proton database. *Nucl. Instrum. Methods Phys. Res. B* **170**, 193–204 (2000).
55. Kondrat, F. D., Struwe, W. B. & Benesch, J. L. Native mass spectrometry: towards high-throughput structural proteomics. *Methods Mol. Biol.* **1261**, 349–371 (2015).
56. Sobott, F., Hernández, H., McCammon, M. G., Tito, M. A. & Robinson, C. V. A tandem mass spectrometer for improved transmission and analysis of large macromolecular assemblies. *Anal. Chem.* **74**, 1402–1407 (2002).
57. Press, W. H., Teukolsky, S. A., Vetterling, W. T. & Flannery, B. P. *Numerical recipes in C: the art of scientific computing* 2nd edn (Cambridge Univ. Press, Cambridge, 1992).
58. Simms, G. A., Padmos, J. D. & Zhang, P. Structural and electronic properties of protein/thiolate-protected gold nanocluster with "staple" motif: A XAS, L-DOS, and XPS study. *J. Chem. Phys.* **131**, 214703 (2009).
59. Zhang, P. & Sham, T. K. X-ray studies of the structure and electronic behavior of alkanethiolate-capped gold nanoparticles: the interplay of size and surface effects. *Phys. Rev. Lett.* **90**, 245502 (2003).
60. Movasaghi, Z., Rehman, S. & Rehman, I. U. Raman spectroscopy of biological tissues. *Appl. Spectrosc. Rev.* **42**, 493–541 (2007).

a

Measurements	PDI*	Mean diameter (nm)†
1	0.074	21.62
2	0.025	22.51
3	0.050	22.25
4	0.020	22.25
5	0.020	22.11
6	0.017	22.23
7	0.044	23.38
8	0.046	22.48
9	0.042	22.50
Mean	0.038	22.26
S.D.	0.019	0.28

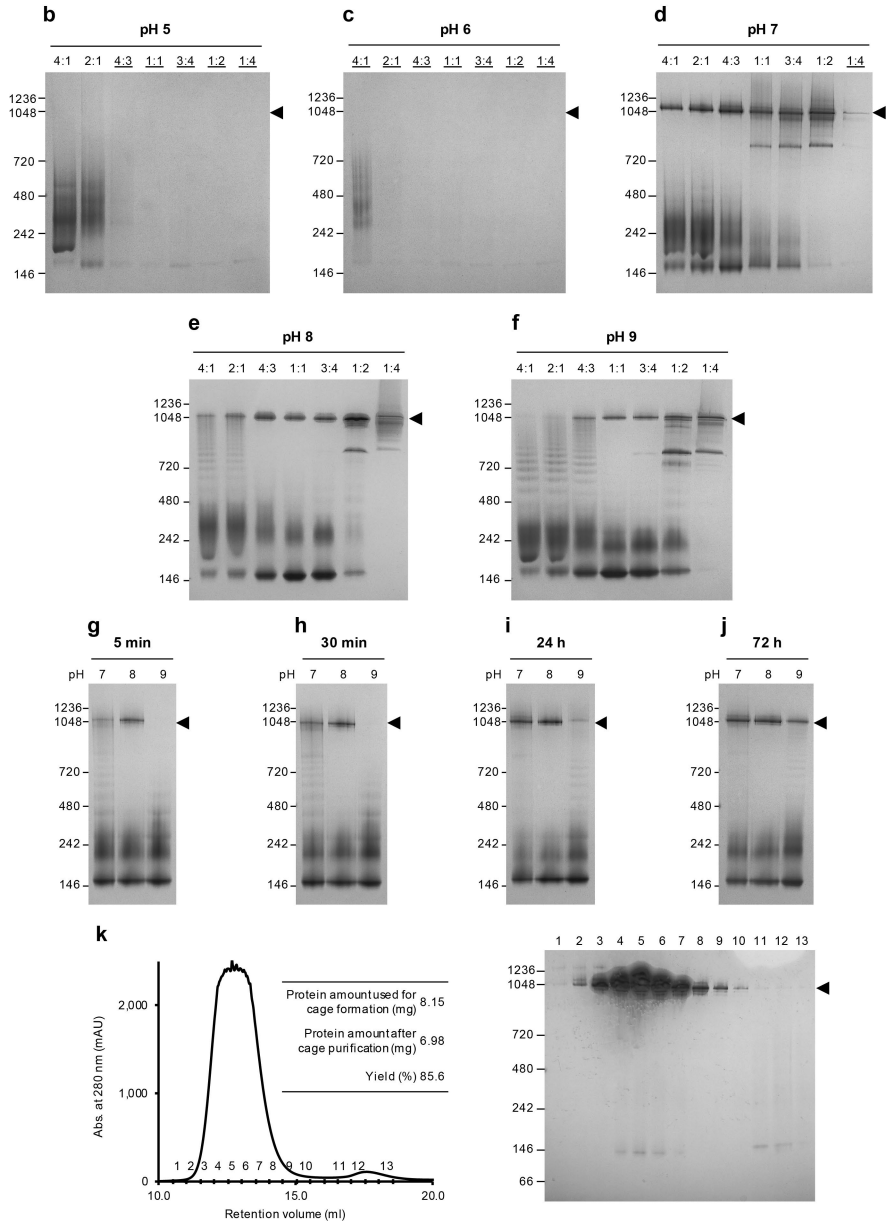

Extended Data Fig. 1 | See next page for caption.

Extended Data Fig. 1 | Size determination and optimization of conditions for TRAP-cage formation. a, Average size of TRAP-cage determined by dynamic light scattering, based on three separate preparations of purified TRAP-cage, each measured in triplicate. PDI, polydispersity index. The mean diameter is based on volume distribution. **b**–**f**, Effect of pH on cage formation. Reactions containing 0.8 mg ml^{-1} TRAP(K35C/R64S) were incubated with Au-TPPMS at the indicated pH values for 3 days, spun down on a desktop centrifuge and subjected to blue native PAGE. The ratios are TRAP(K35C/R64S) monomer:Au(I) molar ratios. Formation of white precipitate was detected in the reactions for which the ratios are underlined, and correlates with a decrease in band intensity. **g**–**j**, Time course of TRAP-cage formation at pH 7, 8 and 9, visualized by blue native PAGE. Each reaction contains Au-TPPMS and 0.8 mg ml^{-1} TRAP(K35C/R64S) at a 1:1 molar ratio. Total incubation times are indicated above each gel. Gels **b**–**j** were repeated once, giving similar results. **k**, Left, the product of reaction containing 8.15 mg TRAP(K35C/R64S) and Au-TPPMS under standard cage-formation conditions was subjected to SEC using a Superose 6 Increase 10/300 GL column and fractions were collected as indicated. Right, native PAGE of fractions 1–13 demonstrates that they contain almost exclusively cage structures. The inset table demonstrates high recovery yields of TRAP-cage based on A_{280} measurements of initial and purified samples. SEC is representative of two independent experiments, giving similar results. Positions of molecular-weight marker bands are indicated to the left of gels and arrowheads indicate the position of bands corresponding to TRAP-cage. For gel source data, see Supplementary Fig. 1.

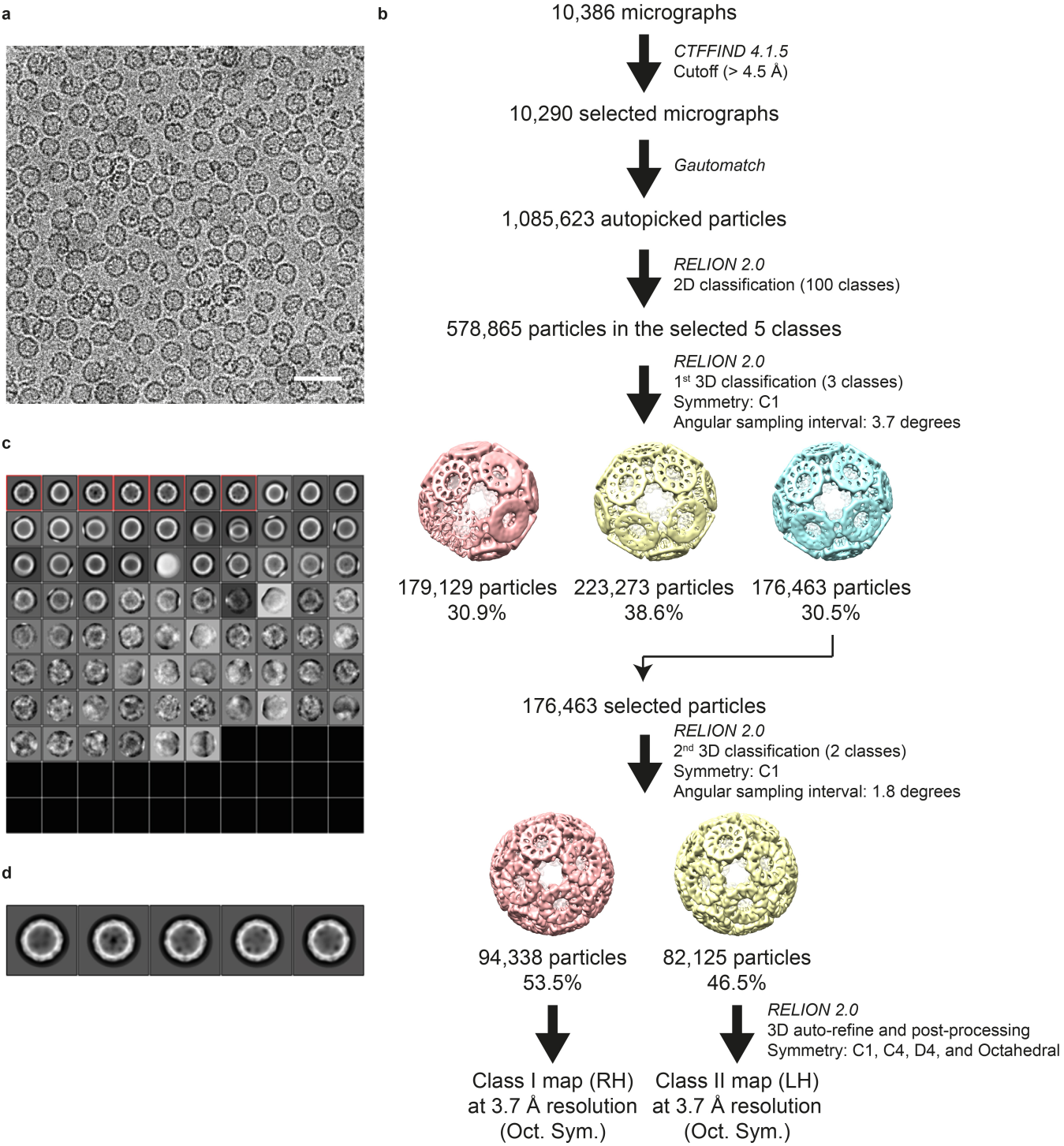

Extended Data Fig. 2 | Procedure for cryo-EM single-particle reconstruction for TRAP-cage formed with Au-TPPMS. **a**, Representative micrograph of the TRAP-cage. Scale bar, 50 nm. **b**, Summary of the image processing procedure (see Methods). **c**, 2D class averages from reference-free 2D classification by RELION 2.0. The selected 2D class-averaged images (5 classes including 578,865 particles) for further image processing are highlighted with red squares. **d**, The selected five 2D classes (box size: 220 × 220 pixels, 382.8 × 382.8 Å).

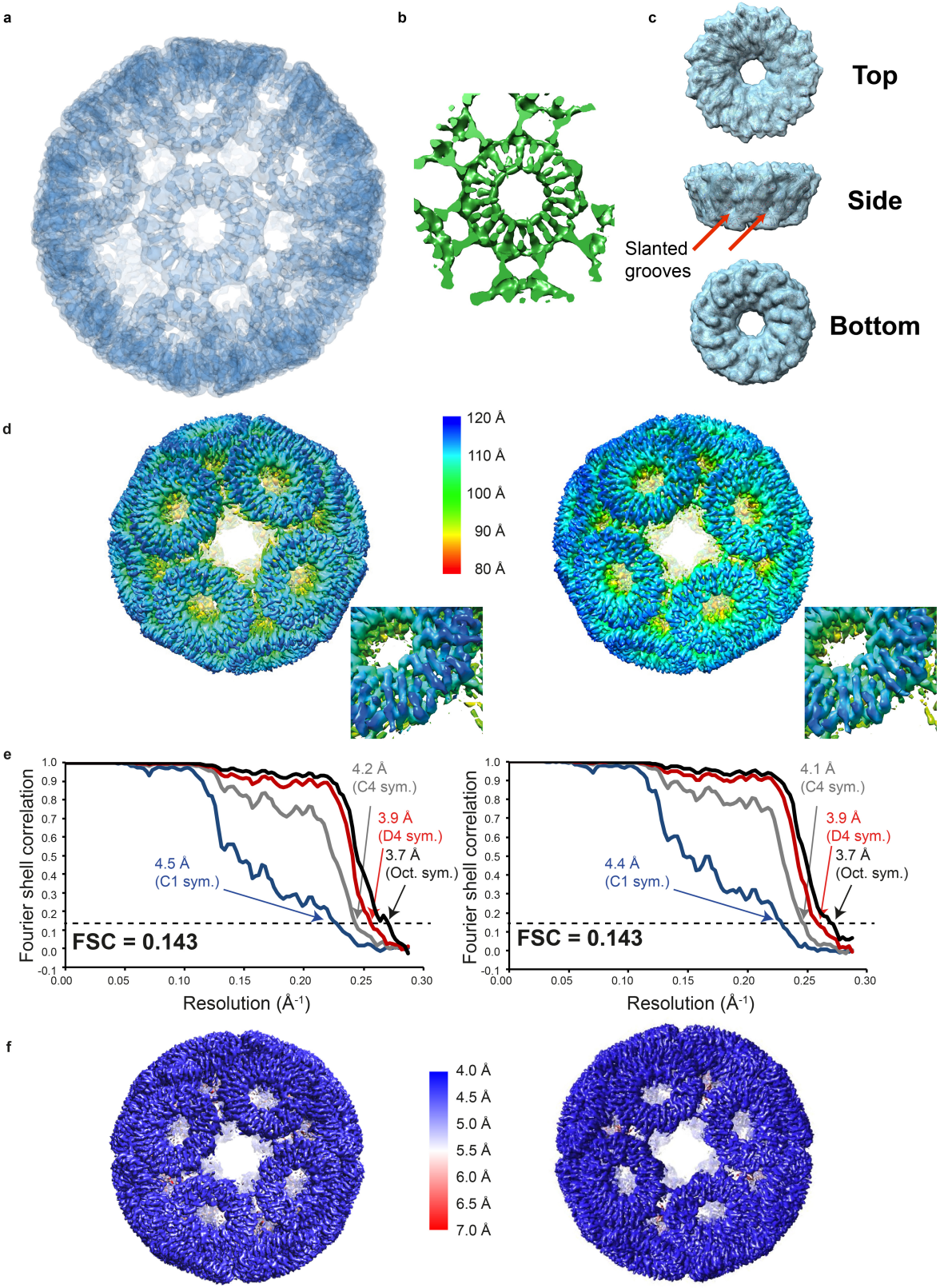

Extended Data Fig. 3 | See next page for caption.

Extended Data Fig. 3 | Initial density map of TRAP-cage displaying aberrant features and final map quality and resolution for TRAP-cage formed with Au-TPPMS. a, **b**, The initial cryo-EM map, refined to 5.6 Å resolution, showing a distinct lack of chirality at the level of the individual rings. **a**, Overall map depicted in transparency, showing ring densities resembling radial wheel spokes. **b**, Magnification of a ring density at low contour level, viewed from the interior of the cage, showing exclusively radial features (densities and gaps). **c**, For comparison, the atomic model of TRAP(K35C/R64S) (based on PDB: 4V4F), is simulated to a resolution of 5.9 Å, showing that chiral properties (for example, curved propeller-like features, slanted grooves) should be readily visible on the rings at this resolution. **d**, **e**, Map quality and resolution of the two final cryo-EM density maps bearing opposite chirality: left-handed and right-handed cages are shown on the left and right, respectively. **d**, Surface representations coloured according to the distance from the centre of the particle. **e**, Gold-standard FSC curve for the cryo-EM map of left-handed and right-handed cages with C1, C4, D4, and octahedral (Oct) symmetries from 82,125 and 94,338 particles, respectively. The estimated resolutions at the 0.143 criterion were 3.7 Å for the two octahedral symmetry maps. **f**, The refined density maps coloured by local resolution in surface view.

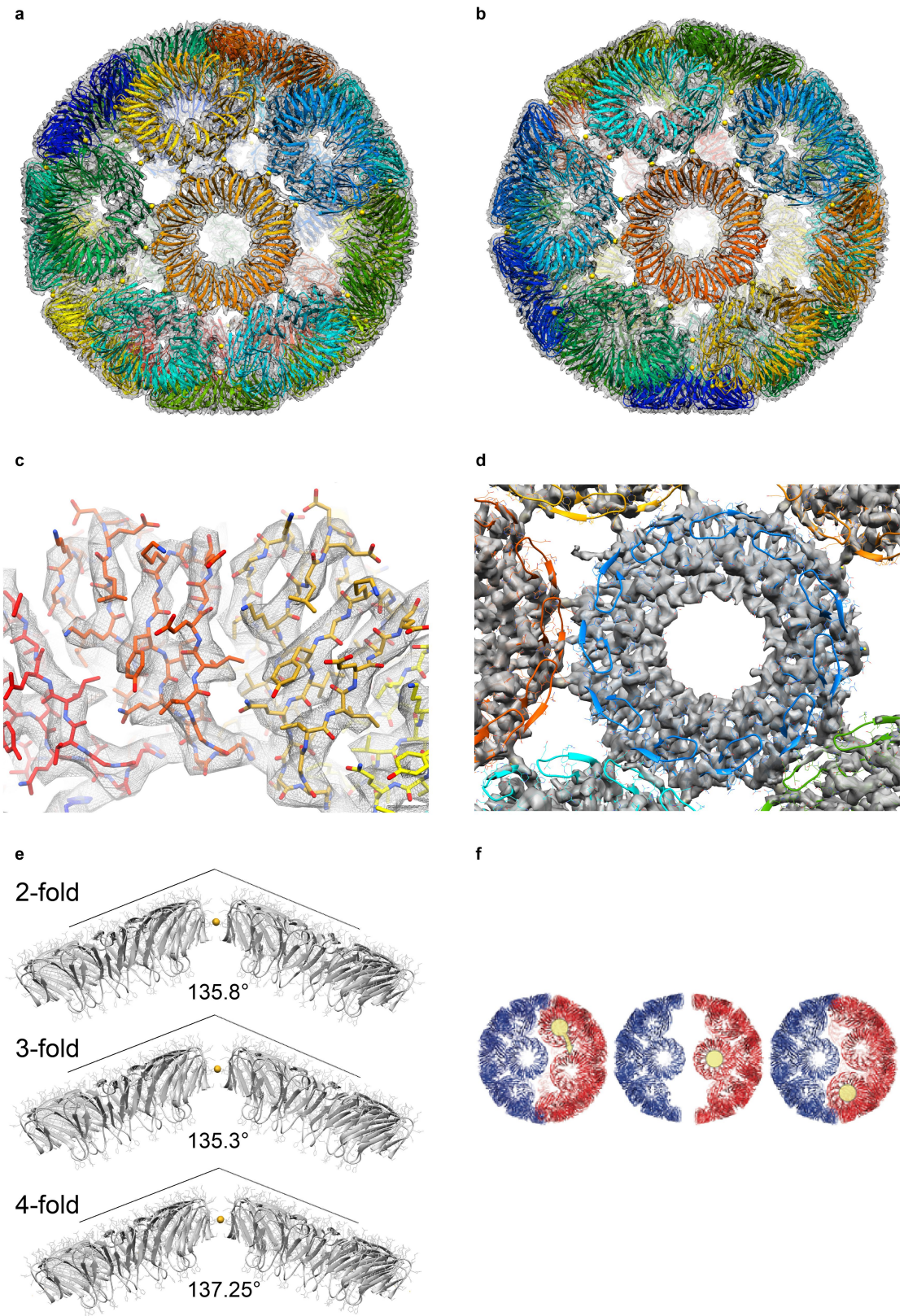

Extended Data Fig. 4 | See next page for caption.

Extended Data Fig. 4 | Details of the refined TRAP-cage structure. **a**, **b**, Overall fits of the final TRAP-cage models onto their respective density maps: left-handed (**a**) and right-handed (**b**) structures. Cysteine residues are rendered as ball and stick models, whereas gold atoms are shown as spheres. **c**, Magnified view of the left-handed cage, to show fitting of TRAP(K35C/R64S) structural elements into the density. **d**, Magnified view of the interior of the left-handed cage, showing flexible loop (residues 22–32) with missing density, consistent with the non-tryptophan-bound TRAP structure[44]. **e**, Slightly unequal dihedral angles are formed between neighbouring TRAP(K35C/R64S) rings in the final TRAP-cage model, averaging 135.8°, 135.3° and 137.25° around the two-, three-, and four-fold rotational axes, respectively, with a mean value of 136.2° across the entire cage. It is notable that in the canonical pentagonal icositetrahedron, a constant dihedral angle of 136.3° is formed between any two adjacent faces. **f**, The equivalence of the two chiral forms of TRAP-cage may explain their roughly equal proportions, and is clear if the cage assemblies are decomposed into two congruent hemispheres of 12 rings each. The hemispheres are themselves achiral, but together two can take either chiral form depending on their relative orientations when assembled. The two chiral forms can be interconverted through the relative rotation of hemispheres by about 24.1°. In the figure, each achiral half of the cage is coloured in red and blue, and the relative rotation can be tracked as the change in position of the highlighted ring in the direction of the arrow.

a

Measurement	Gold concentration (mg/ml)	SD of measurement (mg/ml)	Equivalent no. of Au per cage	SD in no. of Au per cage
1	9.34	0.6	103	7
2	9.23	0.3	102	3
3	9.58	1.0	106	11
4	10.99	0.2	121	2
5	11.12	0.3	123	3

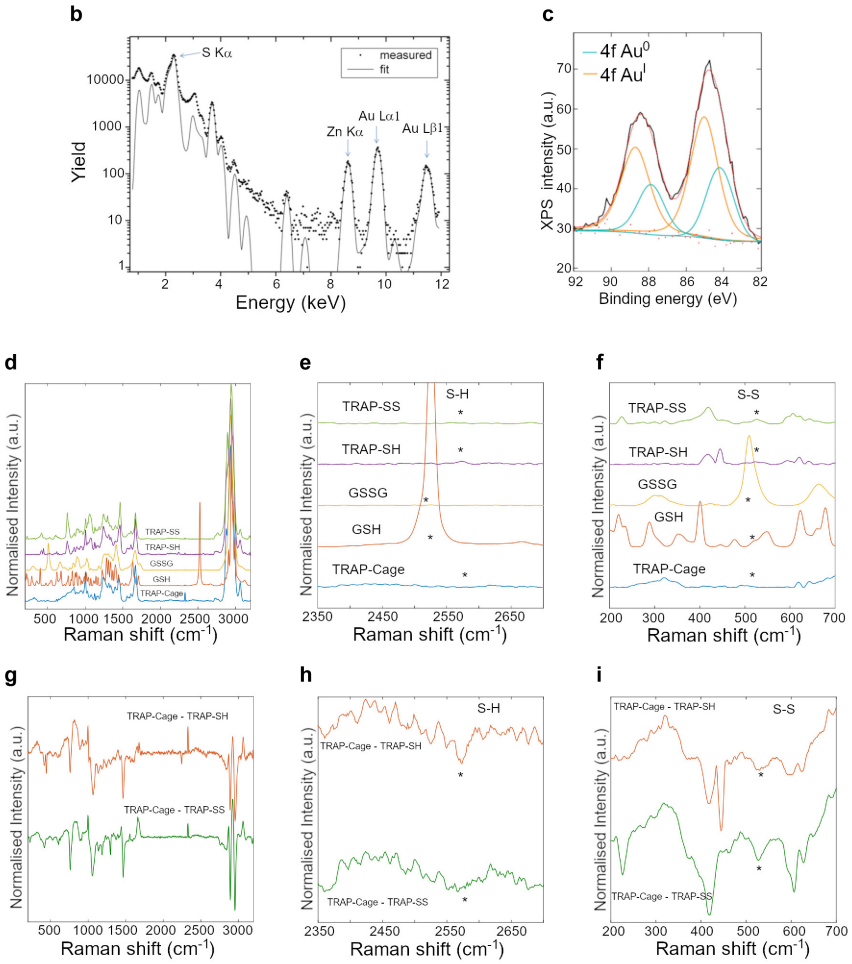

Extended Data Fig. 5 | Confirmation and quantitation of gold in the TRAP-cage. a, Results of five electrothermal atomic absorption spectroscopy measurements of TRAP-cage, each performed in triplicate, showing the measured mass of gold and its translation into the number of gold atoms per TRAP-cage. Measurement 3 was discarded in the calculation of overall averages owing to the large observed error. **b**, Micro-PIXE measurements of purified TRAP-cage showing the X-ray spectrum. Au L peaks and the S K peak were used to estimate the S:Au molar ratio in the sample, which was calculated to a range of approximately 5.1–6.9 S per Au. The dots represent the measured data, whereas the continuous line represents the fit with the Gupixwin program[54]. Results are representative of two independent experiments, each giving similar results. **c**, Au 4*f* XPS spectra (black line) of the TRAP-cage with the expected spectra for Au^0 and Au^I shown in blue and orange, respectively. The cumulative fit (red) and residuals (small red squares) are also shown. The shift in binding energy from 84.19 to 84.99 eV (that is, 0.80 eV) matches well with values for Au–S reported previously[58,59]. The presence of signal in the Au^0 binding-energy range can be attributed to a weakly interacting Au coordination bond with the second sulfur in the bridge, because repeated measurements of different purification methods excluded the chance of X-ray degradation or unreacted substrates giving a Au^0 signal. **d**–**i**, Raman spectroscopy suggests the absence or low abundance of S–S and S–H bonds in TRAP-cage. **d**, Raman spectra of TRAP-cage, oxidized and reduced TRAP-rings (TRAP-SS and TRAP-SH respectively), with oxidized and reduced glutathione (GSSG and GSH, respectively), showing the full spectral range. **e**, **f**, Enlargements of the S–H vibration (**e**) and S–S (**f**) vibration regions. Locations of peaks corresponding to S–S and S–H vibrations are labelled with asterisks. Because the exact positions depend on the molecular species and its conformation, the peak maxima for glutathione are shifted relative to cysteine-based signals (for example, the range for S–S vibrations is 509–540 cm^{-1})[60]. Because some peaks corresponding to S–H and S–S bonds were small, their absence from the TRAP-cage spectra was assessed by subtracting relevant spectra (that is, TRAP-SS or TRAP-SH) for TRAP-rings from the TRAP-cage data. **g**, The resulting spectra shown in the full spectral range. **h**, **i**, Enlargements of the S–H (**h**) and S–S (**i**) regions. Spectra after normalization were offset for clarity. For XPS and Raman spectra, experiments were independently repeated at least once, each giving similar results.

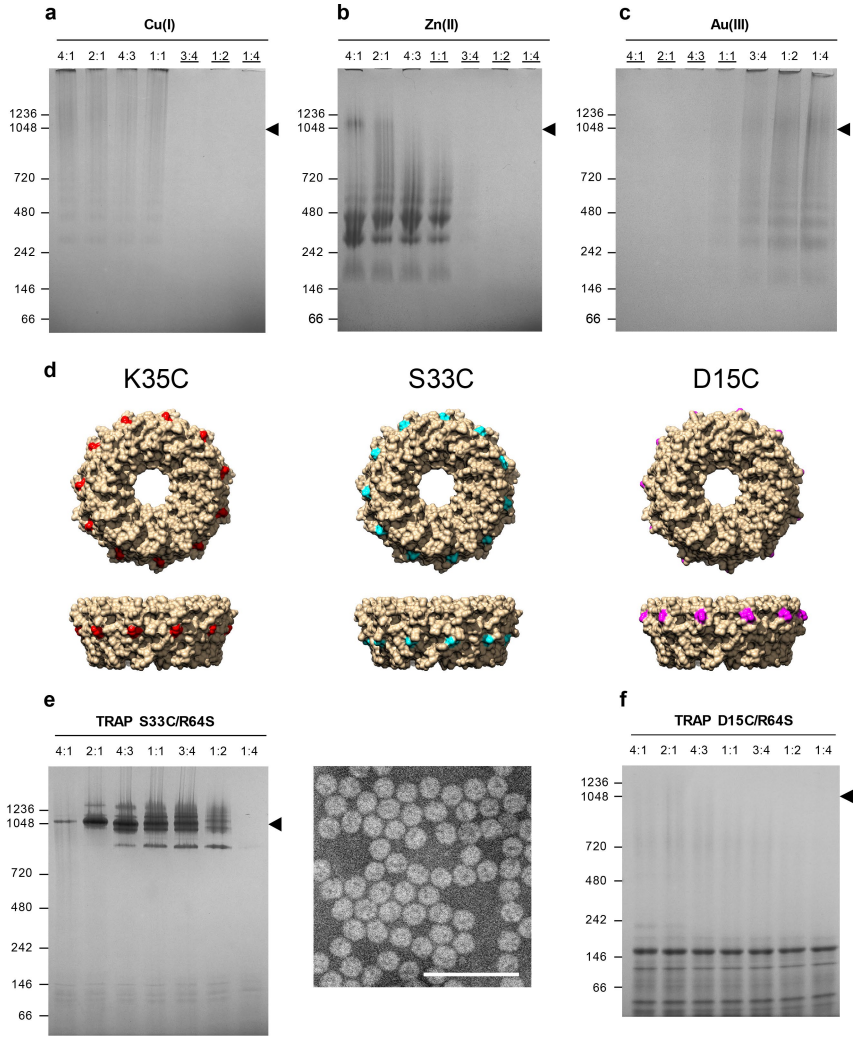

Extended Data Fig. 6 | Further probing TRAP-cage assembly. **a–c**, Testing the ability of different metal ions to induce protein cage formation. Reactions containing 0.8 mg ml^{-1} TRAP(K35C/R64S) were incubated under standard cage-formation conditions, except that Au-TPPMS was replaced with the indicated metal ions, then spun down on a desktop centrifuge and subjected to blue native PAGE. TRAP(K35C/R64S) monomer:metal ion molar ratios are indicated above each lane. TRAP(K35C/R64S) was incubated with Cu^{I} (**a**), Zn^{II} (**b**) and Au^{III} (**c**). White precipitate was detected in the reactions for which the ratios are underlined, and correlates with a decrease in band intensity. **d**, Modelling alternative locations for placement of cysteine residues on the surface of the TRAP ring, based on PDB: 4V4F, and shown in orthogonal views: K35C, S33C and D15C, with the location of the substituted residues rendered in red, cyan and purple, respectively. **e**, Reaction of TRAP(S33C/R64S) with Au-TPPMS produces uniform cage structures, as shown by native PAGE (left) and TEM (right). Scale bar, 100 nm. **f**, Reaction of TRAP(D15C/R64S) with Au-TPPMS fails to produce higher-order structures, as shown by native PAGE. Gels in **a–c**, **e**, **f** and TEM were repeated independently twice, each giving similar results. Positions of molecular-weight markers on gels are indicated and arrowheads indicate position of TRAP-cage produced using Au-TPPMS. For gel source data, see Supplementary Fig. 1.

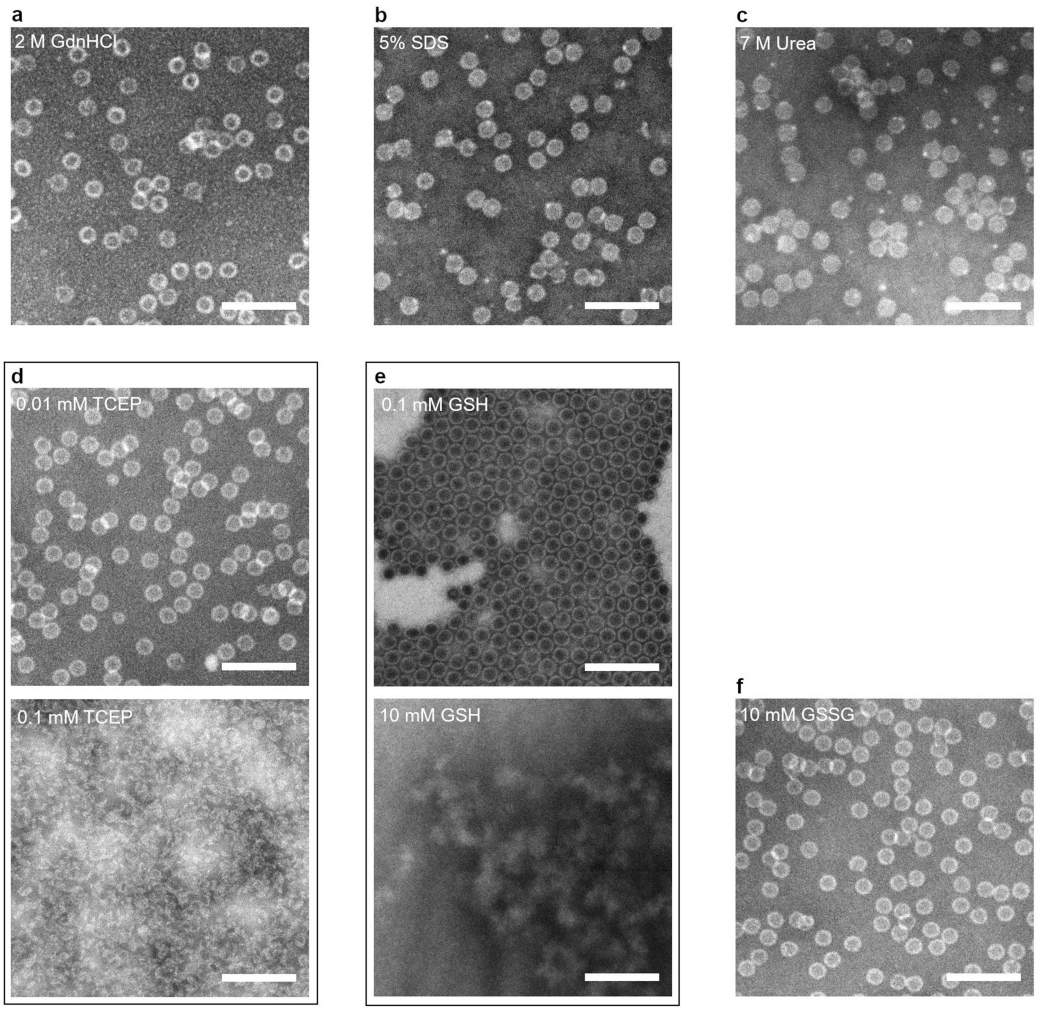

Extended Data Fig. 7 | Additional tests of TRAP-cage stability. TRAP-cage was prepared as for cages in Fig. 1d. Purified TRAP-cage samples were incubated at room temperature overnight in 2 M guanidinium HCl (**a**), 5% SDS (**b**), 7 M urea (**c**), 0.01 and 0.1 mM TCEP (**d**), 0.1 and 10 mM GSH (**e**) and 10 mM GSSG (**f**), and subsequently imaged under TEM. All TEM images shown are representative of data that was repeated once, each giving similar results. Scale bars, 100 nm.

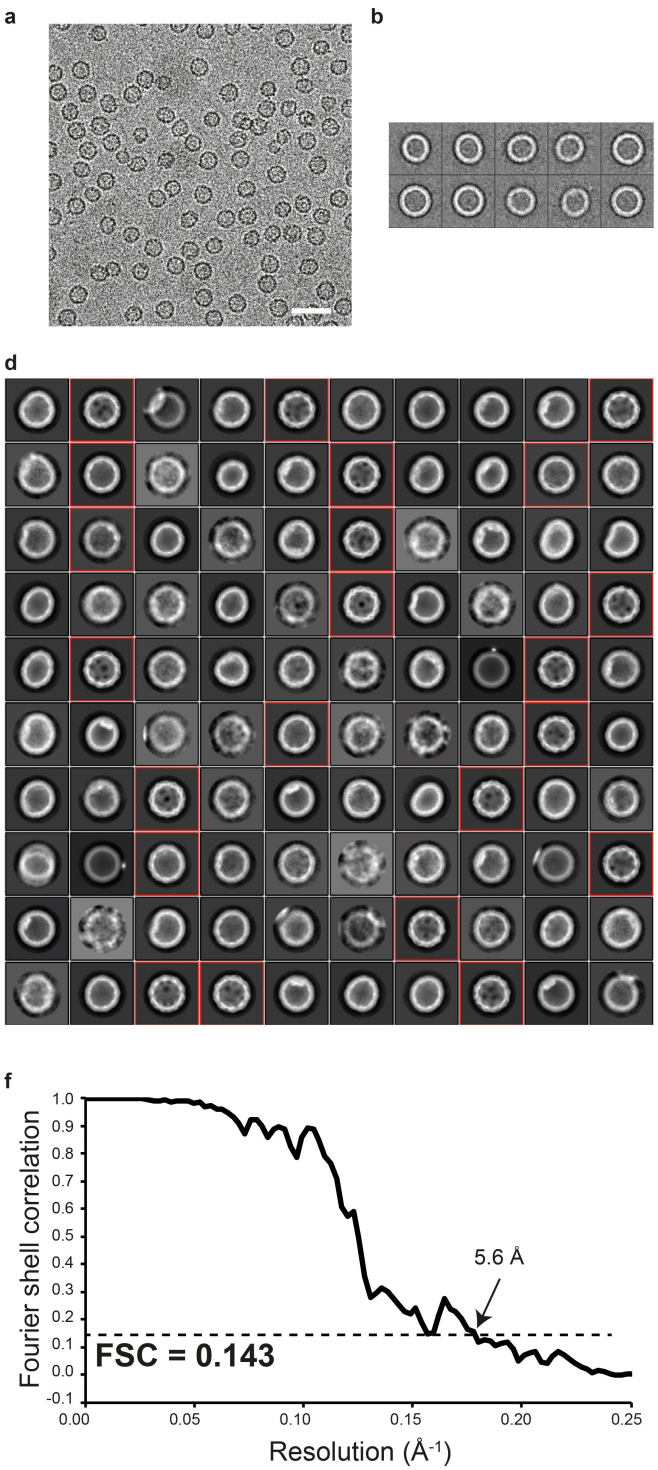

Extended Data Fig. 8 | Procedure for cryo-EM single-particle reconstruction, map quality and resolution for TRAP-cage formed with GNP. a, A representative micrograph of the TRAP-cage formed using GNP. Scale bar, 50 nm. **b**, Images of selected 2D classes from reference-free 2D classification by EMAN 2.1, used for automated particle picking with Gautomatch (box size: 220 × 220 pixels, 400.4 × 400.4 Å). **c**, Summary of the image processing procedure (see Methods). **d**, 2D class averages from reference-free 2D classification by RELION 2.0. The selected 2D class averages (22 images) for further image processing are highlighted with red squares. It is notable that in some cases (for example, row 1 panel 9) structures inside the TRAP-cage are visible, probably reflecting stochastic capture of TRAP rings as cargo in the cage interior. **e**, Initial structure used for the high-resolution analysis. The surface representations are coloured according to the distance from the centre of the particle. **f**, Gold-standard FSC curve for the cryo-EM map from 58,157 particles. The calculated spatial frequency at the 0.143 criterion was 5.6 Å. **g**, The refined density map coloured by local resolution in surface and slice views.

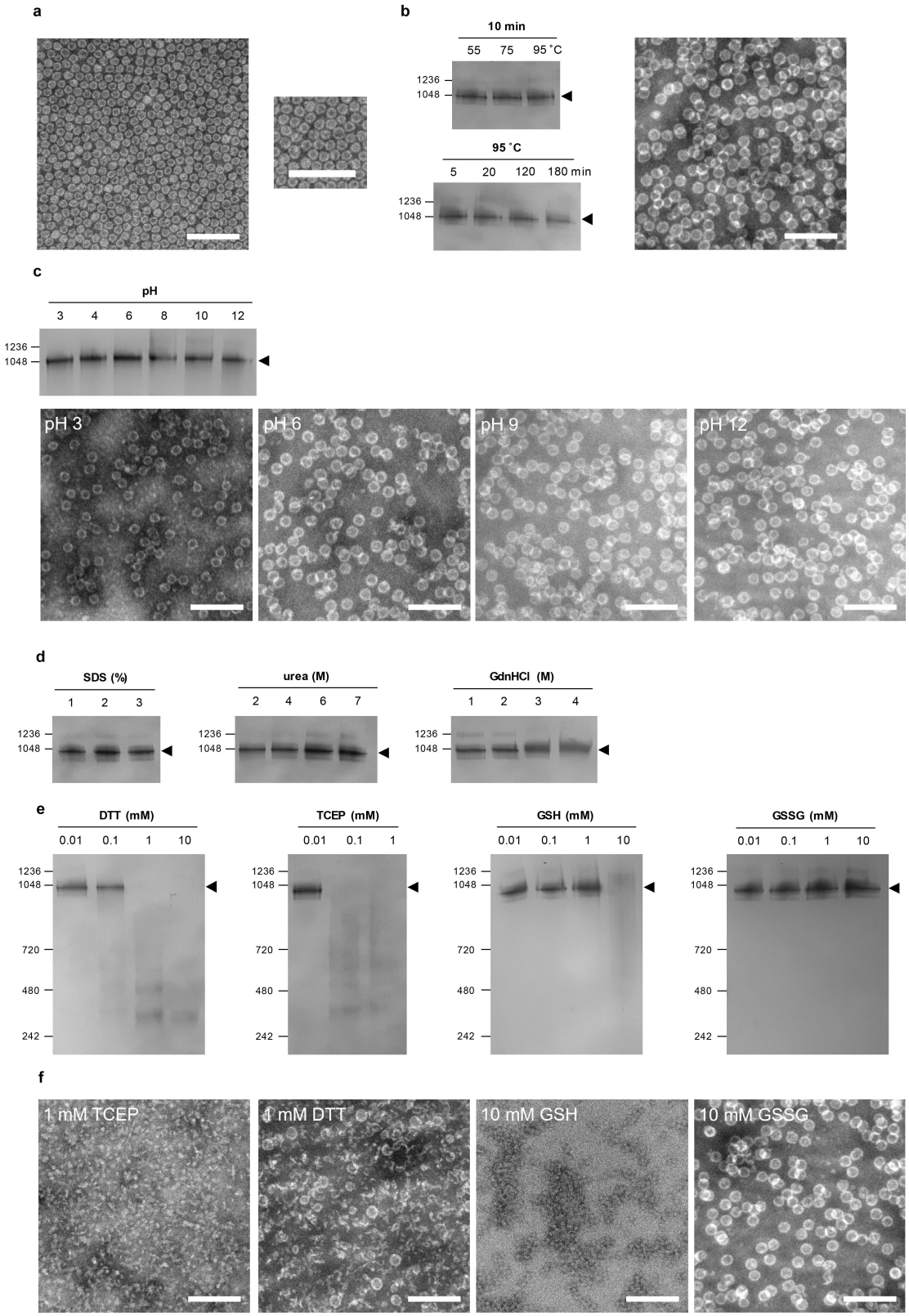

Extended Data Fig. 9 | Formation and stability of TRAP-cage formed with GNPs (TRAP-cage(GNP)). TRAP-cages were formed under GNP-cage formation conditions (see Methods). **a**, TEM image of purified TRAP-cage(GNP), with a magnified view on the right. **b**, Thermal stability of TRAP-cage(GNP) upon incubation at the indicated temperatures and times. The TEM image shows that structural integrity is maintained after incubation at 95 °C for 180 min. **c**, Stability of TRAP-cage(GNP) as a function of pH. **d**, Stability of TRAP-cage(GNP) upon the addition of different chaotropic agents: SDS, urea and guanindine HCl. **e**, **f**, Reducing agents trigger disassembly of TRAP-cage(GNP), as shown by native PAGE (**e**) and TEM (**f**). Assay conditions are indicated above each lane on the gel. Positions of molecular weight markers are indicated and arrowheads show the position of TRAP-cage. For TEM, scale bars are 100 nm. All gels and TEM images shown are representative of experiments repeated independently at least once, each giving similar results. For gel source data, see Supplementary Fig. 1.

Extended Data Table 1 | Cryo-EM data collection, refinement and validation statistics

	LH TRAP-cage (EMDB-4443) (PDB 6IB3)	RH TRAP-cage (EMDB-4444) (PDB 6IB4)
Data collection and processing		
Magnification	75000	75000
Voltage (kV)	300	300
Electron exposure (e–/Å^2)	40	40
Defocus range (μm)	-0.9 ÷ -3.4	-0.9 ÷ -3.4
Pixel size (Å)	0.87	0.87
Symmetry imposed	Oh	Oh
Initial particle images (no.)	10386	10386
Final particle images (no.)	10290	10290
Map resolution (Å)	3.7	3.7
FSC threshold	0.143	0.143
Map resolution range (Å)	3.0 ÷ 7.0	3.0 ÷ 7.0
Refinement		
Initial model used (PDB code)	4v4f	4v4f
Model resolution (Å)	3.8	3.8
Map sharpening *B* factor (Å^2)	-236	-244
Model composition		
Non-hydrogen atoms	135552	135552
Protein residues	17688	17688
Ligands	120	120
B factors (Å^2)		
Protein	64.65	61.07
Ligand	219.22	210.12
R.m.s. deviations		
Bond lengths (Å)	0.08	0.06
Bond angles (°)	0.656	0.596
Validation		
MolProbity score	0.93	1.02
Clashscore	1.72	2.43
Poor rotamers (%)	0	0
Ramachandran plot		
Favored (%)	98.04	98.04
Allowed (%)	1.96	1.96
Disallowed (%)	0	0

nature research

Corresponding author(s): Jonathan G. Heddle

Reporting Summary

Nature Research wishes to improve the reproducibility of the work that we publish. This form provides structure for consistency and transparency in reporting. For further information on Nature Research policies, see Authors & Referees and the Editorial Policy Checklist.

Statistical parameters

When statistical analyses are reported, confirm that the following items are present in the relevant location (e.g. figure legend, table legend, main text, or Methods section).

n/a	Confirmed	
☐	☒	The exact sample size (*n*) for each experimental group/condition, given as a discrete number and unit of measurement
☐	☒	An indication of whether measurements were taken from distinct samples or whether the same sample was measured repeatedly
☒	☐	The statistical test(s) used AND whether they are one- or two-sided *Only common tests should be described solely by name; describe more complex techniques in the Methods section.*
☒	☐	A description of all covariates tested
☐	☒	A description of any assumptions or corrections, such as tests of normality and adjustment for multiple comparisons
☐	☒	A full description of the statistics including central tendency (e.g. means) or other basic estimates (e.g. regression coefficient) AND variation (e.g. standard deviation) or associated estimates of uncertainty (e.g. confidence intervals)
☒	☐	For null hypothesis testing, the test statistic (e.g. *F*, *t*, *r*) with confidence intervals, effect sizes, degrees of freedom and *P* value noted *Give P values as exact values whenever suitable.*
☒	☐	For Bayesian analysis, information on the choice of priors and Markov chain Monte Carlo settings
☒	☐	For hierarchical and complex designs, identification of the appropriate level for tests and full reporting of outcomes
☒	☐	Estimates of effect sizes (e.g. Cohen's *d*, Pearson's *r*), indicating how they were calculated
☐	☒	Clearly defined error bars *State explicitly what error bars represent (e.g. SD, SE, CI)*

Our web collection on statistics for biologists may be useful.

Software and code

Policy information about availability of computer code

Data collection	For Gels: No software was used For Size-Exlcusion Chromatography: UNICORN start 1.1, Build 1.1.0.2 (GE); UNICORN 5.20, Build 500 - Workstation (GE) For Electrothermal Atomic Absorption Spectrometry (ET-AAS): Pye Unicam 9100X (Philips) For PIXE: Oxford Microbeams Ltd. Data AcQuisition System (OM_DAQ), Version 5.3, September 2004 For RAMAN: WiRE 4.2 software for Renishaw inVia Raman spectrometer For Cryo-EM : FEI EPU software version 1.9.16REL, For MS : Xcailbur 2.2 (Thermo Scientific), MassLynx V4.1 (Waters) For XPS: SmartSoft 2.8.0.30 (PHI VersaProbe II) For Mass Photometry: Custom iSCAT acquisition software, can be made available on request
Data analysis	For 3D visualizations of shapes :Rhinoceros 3D version 5.5.2 For PIXE: GupixWin, Version 2.1.4, Copyright (C) 2005, University of Guelph For RAMAN: OPUS 7.5 for data manipulation and Matlab 9.3 for final plotting For Cryo-EM : EMAN2 for manual particle picking, Gautomatch for particle auto-picking, Relion version 1.3, 1.4, and 2.0 for 3D reconstruction , Phenix for atomic model refinement, MotionCor2 1.1.0, CTFFIND 4.1.5, Gautomatch, 0, EMAN 1.9, EMAN 2.1, UCSF Chimera 1.13, COOT, Phenix, MolProbity, ResMap 1.1.4, Bsoft 2.0.0, PDBePISA For MS : Xcailbur 2.2 (Thermo Scientific), MassLynx V4.1 (Waters) C++ and Python code used for calculating optimal arrangement of TRAP rings and their visualisation respectively are available upon request.

For XPS: PHI MultiPak program (version 9.8.0.19)
For Mass Photometry: Custom iSCAT analysis software, can be made available on request

For manuscripts utilizing custom algorithms or software that are central to the research but not yet described in published literature, software must be made available to editors/reviewers upon request. We strongly encourage code deposition in a community repository (e.g. GitHub). See the Nature Research guidelines for submitting code & software for further information.

Data

Policy information about availability of data

All manuscripts must include a data availability statement. This statement should provide the following information, where applicable:

- Accession codes, unique identifiers, or web links for publicly available datasets
- A list of figures that have associated raw data
- A description of any restrictions on data availability

The data that support the findings of this study are available via the corresponding author on reasonable request. The cryo-EM density maps have been deposited in the Electron Microscopy Data Bank under accession codes EMD-6966 (GNP-produced TRAP-cage), EMD-4443 (Left-handed TRAP-cage) and EMD-4444 (right-handed TRAP-cage) the coordinates have been deposited in the Protein Data Bank under accession numbers 6IB3 (left-handed TRAP-cage) and 6IB4 (right-handed TRAP-cage).

Field-specific reporting

Please select the best fit for your research. If you are not sure, read the appropriate sections before making your selection.

☒ Life sciences ☐ Behavioural & social sciences

For a reference copy of the document with all sections, see nature.com/authors/policies/ReportingSummary-flat.pdf

Life sciences

Study design

All studies must disclose on these points even when the disclosure is negative.

Sample size	No statistical methods were used to determine sample sizes as samples were derived from proteins in bulk solution and sample size was used as appropriate for each analysis method. For ET-AAS: lyophilized protein sample was divided into small portions (~2mg per sample) and the portions were dissolved in 25 milliliters of 0.2% HCl. Prior measurement, samples were diluted 25-fold. For PIXE: Dried protein patches from two consecutive depositions of 0.5 micro-liters, deposited on 100 nanometer thick pioloform membrane. Diameter of patch area containing dried material is up to approx. 2 millimeters. Maximum size of the scanning field with 3 MeV proton beam at JSI microprobe is 2000 x 2000 µm2. The size of the applied droplets (0.5 microliter) with the protein solution is chosen to cover an area smaller than this size. The number of the droplet applications and consecutive drying was chosen to provide in total protein sample quantity of 1 to 5 micrograms of protein, in compliance with the guidelines provided in the paper of Garman and Grime (see Methods references). For size exclusion chromatography native PAGE gels, negative stain TEM, MS, Cryo-EM, Raman Spectroscopy, XPS and PIXE experiments, protein sample was applied in or produced from protein sample in solution typically in 10s to 100s of µM of protein in µl volumes. For Cryo-EM analysis: 3 uL of each sample solution was applied to cryo-EM grids. In the high resolution structural analysis, approx. one million particles were extracted from approx. 10 thousand micrographs. The sample size was finally determined by the 3D structure based on the reconstituted cryo-EM map that is no worse than 4.0 A by gold-standard Fourier Shell Correlation (FSC) measurement. For Mass Photometry: 5 uL aliquots were taken at 9 time points from a 100 uM sample and measured at 2.5 uM. Sample size was determined to be adequate based on the magnitude and consistency of measurable differences between different experiments, as well as the agreement of the overall results when compared with alternative techniques used to characterise assembly kinetics.
Data exclusions	For ET-AAS: One of the five sets measurements was excluded due to large error in the measurement, these criteria were not pre-established. For all other methods: No data was excluded
Replication	For ET-AAS: Five independent measurements were carried out, each one consisting of three sets of repeats and findings are coincidental For PIXE: Two independent experiments were carried out and findings were reproducible. For gel-based results, negative stain TEM and size exclusion chromatography experiments shown carried out a minimum of two times and findings were reproducible. For RAMAN: All compounds were measured in a duplicate at 2-3 different locations yielding reproducible spectra. For MS: Protein samples were analysed in triplicate, giving similar results For XPS: The TRAP-cage was measured in a duplicate, giving similar results. For Mass Photometry: The sample was measured in duplicate, with the lowest noise images used.
Randomization	n/a as no animal or and human research was carried out in this study and experiments were carried out on known samples.

Blinding | n/a as no animal or and human research was carried out in this study and experiments were carried out on known samples.

Materials & experimental systems

Policy information about availability of materials

n/a	Involved in the study
☐	☒ Unique materials
☒	☐ Antibodies
☒	☐ Eukaryotic cell lines
☒	☐ Research animals
☒	☐ Human research participants

Unique materials

Obtaining unique materials | Plasmids encoding modified TRAP protein are available from the authors upon reasonable request.

Method-specific reporting

n/a	Involved in the study
☒	☐ ChIP-seq
☒	☐ Flow cytometry
☒	☐ Magnetic resonance imaging